



**HAL**  
open science

# Nonlinear seismic response for the 2011 Tohoku earthquake: borehole records versus 1Directional - 3Component propagation models

Maria Paola Santisi d'Avila, Jean-François Semblat

► **To cite this version:**

Maria Paola Santisi d'Avila, Jean-François Semblat. Nonlinear seismic response for the 2011 Tohoku earthquake: borehole records versus 1Directional - 3Component propagation models. *Geophysical Journal International*, 2014, pp.1-15. 10.1093/gji/ggu004 . hal-00943659

**HAL Id: hal-00943659**

**<https://hal.science/hal-00943659>**

Submitted on 8 Feb 2014

**HAL** is a multi-disciplinary open access archive for the deposit and dissemination of scientific research documents, whether they are published or not. The documents may come from teaching and research institutions in France or abroad, or from public or private research centers.

L'archive ouverte pluridisciplinaire **HAL**, est destinée au dépôt et à la diffusion de documents scientifiques de niveau recherche, publiés ou non, émanant des établissements d'enseignement et de recherche français ou étrangers, des laboratoires publics ou privés.

1 **Nonlinear seismic response for the 2011 Tohoku earthquake:**  
2 **borehole records versus 1Directional - 3Component propagation models**

3

4 Maria Paola Santisi d'Avila<sup>1</sup> and Jean-François Semblat<sup>2</sup>

5

6 <sup>1</sup> *Université de Nice-Sophia Antipolis, LJAD, 06108 Nice, France. Email: msantisi@unice.fr*

7 <sup>2</sup> *Université Paris Est, IFSTTAR/GERS/SV, 77447 Marne la Vallée, France.*

8

9 Accepted *date*. Received *date*; in original form *date*

10

11 Abbreviate title: **1D-3C seismic response during the Tohoku earthquake**

12

13 Corresponding author:

14 Maria Paola Santisi d'Avila

15 Laboratoire Jean Alexandre Dieudonné

16 University of Nice Sophia Antipolis

17

18 Address: 28, Avenue de Valrose - 06108 Nice - France

19 Phone: +33(0)4 92 07 62 33

20 Email: msantisi@unice.fr

21

22

23

24 **SUMMARY**

25 The seismic response of surficial multilayered soils to strong earthquakes is analyzed through a  
26 nonlinear one-directional three-component (1D-3C) wave propagation model. The three  
27 components (3C-polarization) of the incident wave are simultaneously propagated into a  
28 horizontal multilayered soil. A 3D nonlinear constitutive relation for dry soils under cyclic  
29 loading is implemented in a quadratic line finite element model. The soil rheology is modeled by  
30 mean of a multi-surface cyclic plasticity model of the Masing-Prandtl-Ishlinskii-Iwan type. Its  
31 major advantage is that the rheology is characterized by few nonlinear parameters commonly  
32 available. Previous studies showed that, when comparing one to three component unidirectional  
33 wave propagation simulations, the soil shear modulus decreases and the dissipation increases, for  
34 a given maximum strain amplitude. The 3D loading path due to the 3C-polarization leads to  
35 multiaxial stress interaction that reduces soil strength and increases nonlinear effects.  
36 Nonlinearity and coupling effects between components are more obvious with decreasing  
37 seismic velocity ratio in the soil and increasing vertical to horizontal component ratio for the  
38 incident wave. This research aims at comparing computed ground motions at the surface of soil  
39 profiles in the Tohoku area (Japan) with 3C seismic signals recorded during the 2011 Tohoku  
40 earthquake. The 3C recorded downhole motion is imposed as boundary condition at the base of  
41 soil layer stack. Notable amplification phenomena are shown, comparing seismograms at the  
42 bottom and at the surface. The 1D-3C approach evidences the influence of the 3D loading path  
43 and input wavefield polarization. 3C motion and 3D stress and strain evolution are evaluated all  
44 over the soil profile. The triaxial mechanical coupling is pointed out by observing the variation  
45 of the propagating wave polarization all along the duration of seismograms. The variation of the  
46 maximum horizontal component of motion with time, as well as the influence of the vertical

47 component, confirm the interest of taking into account the 3C nonlinear coupling in 1D wave  
48 propagation models for such a large event.

49

## 50 **KEYWORDS**

51 Earthquake ground motions, Site effects, Wave propagation, Computational seismology.

52

## 53 **1 INTRODUCTION**

54 Surficial soil layers act as a filter on propagating seismic waves, changing the frequency content,  
55 duration and amplitude of motion. Amplification phenomena depend on path layering, velocity  
56 contrast and wave polarization (Bard & Bouchon 1985). Furthermore, seismic waves due to  
57 strong ground motions propagating in surficial soil layers may both reduce soil stiffness and  
58 increase nonlinear effects. The nonlinear behavior of the soil may have beneficial or detrimental  
59 effects on the dynamic response at the surface, depending on the energy dissipation process. The  
60 three-dimensional (3D) loading path influences the stresses into the soil and thus its seismic  
61 response.

62 This research aims at providing a model to study the local seismic response in case of strong  
63 earthquakes affecting alluvial sites. The proposed approach allows to assess possible  
64 amplifications of seismic motion at the surface, influenced by the geological and geotechnical  
65 structure. Such parameters as the three-component motion and 3D stress and strain states along  
66 the soil profiles may thus be computed in order to investigate in deeper details the effects of soil  
67 nonlinearity, seismic wave polarization and multiaxial coupling under 3C cyclic motion.

68 Past studies have been devoted to one-directional shear wave propagation in a multilayered soil  
69 profile (1D-propagation) considering one motion component only (1C-polarization). One-

70 directional wave propagation analyses are an easy way to investigate local seismic hazard for  
71 strong ground motions. Several 1D propagation models were developed, to evaluate the 1C  
72 ground response of horizontally layered sites, reproducing soil behavior as equivalent linear  
73 (SHAKE, Schnabel *et al.* 1972; EERA, Bardet *et al.* 2000; Kausel & Assimaki, 2002), dry  
74 nonlinear (NERA, Bardet *et al.* 2001, X-NCQ, Delépine *et al.* 2009) and saturated nonlinear  
75 (DESRA-2, Lee & Finn 1978; TESS by Pyke 2000 from PEERC 2008; DEEPSOIL, Hashash  
76 and Park 2001; DMOD2, Matasovic 2006). The 1D-1C approach is a good approximation in the  
77 case of low strains within the linear range (superposition principle, Oppenheim *et al.* 1997). The  
78 effects of axial-shear stress interaction in multiaxial stress states have to be taken into account  
79 for higher strain levels, in the nonlinear range. The main difficulty is to find a constitutive model  
80 that reproduces faithfully the nonlinear and hysteretic behavior of soils under cyclic loadings,  
81 with the minimum number of parameters characterizing soil properties. Moreover, representing  
82 the 3D hysteretic behavior of soils, to reproduce the soil dynamic response to a three-component  
83 (3C) wave propagation, means considering three motion components that cannot be computed  
84 separately (SUMDES code, Li *et al.* 1992; SWAP\_3C code, Santisi d'Avila *et al.* 2012, 2013).  
85 Li (1990) incorporated the 3D cyclic plasticity soil model proposed by Wang *et al.* (1990) in a  
86 1D finite element procedure (Li *et al.* 1992), in terms of effective stress, to simulate the one-  
87 directional wave propagation accounting for pore pressure in the soil. However, this complex  
88 rheology needs a large number of parameters to characterize the soil model at field sites.  
89 In this research, the specific 3D stress-strain problem for seismic wave propagation along one-  
90 direction only (1D-3C approach) is solved using a constitutive model of the Masing-Prandtl-  
91 Ishlinskii-Iwan (MPII) type (Iwan 1967, Joyner 1975, Joyner & Chen 1975), as called by  
92 Segalman & Starr (2008), depending only on commonly measured properties: mass density,

93 shear and pressure wave velocities and the nonlinear shear modulus reduction versus shear strain  
94 curve. Due to its 3D nature, the procedure can handle both shear wave and compression wave  
95 simultaneously and predict the ground motion taking into account the wave polarization.

96 Most of previously mentioned one-directional one-component (1D-1C) time domain nonlinear  
97 approaches use lumped mass (DESRA-2, Lee & Finn 1978; DEEPSOIL, Hashash and Park  
98 2001; DMOD2, Matasovic 2006) or finite difference models (TESS by Pyke 2000 from PEERC  
99 2008). In this research, the MPII constitutive model is implemented in a finite element scheme,  
100 allowing the evaluation of seismic ground motion due to three-component strong earthquakes  
101 and proving the importance of a three-directional shaking modelling.

102 According to Santisi *et al.* (2012), the main difference between three superimposed one-  
103 component ground motions (1D-1C approach) and the proposed one-directional three-  
104 component propagation model (1D-3C approach) is observed in terms of ground motion time  
105 history, maximum stress and hysteretic behavior, with more nonlinearity and coupling effects  
106 between components. These consequences are more obvious with decreasing seismic velocity  
107 ratio (and Poisson's ratio) in the soil and increasing vertical to horizontal component ratio of the  
108 incident wave.

109 Santisi d'Avila *et al.* (2012, 2013) investigated the influence of soil properties, soil profile  
110 layering and 3C-quake features on the local seismic response of multilayered soil profiles,  
111 applying an absorbing boundary condition at the soil-bedrock interface (Joyner & Chen 1975),  
112 in the 1D-3C wave propagation model. The same elastic bedrock modelling was adopted by Lee  
113 & Finn (1978), Li (1990) and Bardet *et al.*, (2000, 2001). Halved seismograms recorded at the  
114 top of close outcropping rock type profiles are applied as 3C incident wave in analyzed soil  
115 profiles. The accuracy of predicted soil motion depends significantly on the rock motion

116 characteristics. This kind of procedure cannot be proposed for design, criteria for choosing  
117 associated rock motions not being known precisely (PEERC 2008).

118 In the present research, the goal is to appraise the reliability of the 1D-3C propagation model  
119 using borehole seismic records. In this case, the 3C signal contains incident and reflected waves,  
120 so an imposed motion at the base of the soil profile is more adapted as boundary condition. The  
121 validation of the proposed 1D-3C propagation model is undertaken comparing the three-  
122 component signals of the 11 March 2011 Mw 9 Tohoku earthquake, recorded at the surface of  
123 alluvial deposits in the Tohoku area (Japan), with the numerical time histories at the top of  
124 stacked horizontal soil layers. Seismic records with high vertical to horizontal acceleration ratio  
125 are applied in this research, to investigate the impact of such large ratios. Soil and quake  
126 properties are related to the same profile, increasing the accuracy of results and consequently  
127 allowing more quantitative analyses.

128 The proposed 1D-3C wave propagation model with a boundary condition in acceleration at  
129 depth is presented in Section 2. Soil properties and quake features for the analyzed cases are  
130 presented in Section 3. Anderson's criteria (Anderson 2004) are used to assess the reliability of  
131 the proposed model in Section 4, estimating the goodness of fit of synthetic signals compared  
132 with seismic records. In this section, hysteretic loops and component ration are also computed.

133 The conclusions are developed in Section 5.

134

## 135 **2 1D-3C PROPAGATION MODEL USING BOREHOLE RECORDS**

136 The three components of seismic motion are propagated along one direction in nonlinear soil  
137 stratification. The multilayered soil is assumed infinitely extended along the horizontal  
138 directions. The wide extension of alluvial basins induces negligible surface wave effects

139 (Semblat & Pecker, 2009). Shear and pressure waves propagate vertically in the  $z$ -direction.  
140 These hypotheses yield no strain variation in the  $x$ - and  $y$ -direction. At a given depth, the soil  
141 is assumed to be a continuous, isotropic and homogeneous medium. Small and medium strain  
142 levels are considered during the process.

143

## 144 **2.1 3D nonlinear hysteretic model**

145 The adopted Masing-Prandtl-Ishlinskii-Iwan rheological model for soils (Bertotti & Mayergoyz  
146 2006; Segalman & Starr 2008) is suggested by Iwan (1967) and applied by Joyner (1975) and  
147 Joyner & Chen (1975) in a finite difference formulation. It has been selected because it emulates  
148 a 3D behavior, nonlinear for both loading and unloading and, above all, because the only  
149 necessary parameter to characterize the soil hysteretic behavior is the shear modulus decay  
150 curve  $G(\gamma)$  versus shear strain  $\gamma$ .

151 The soil nonlinearity reduces the shear modulus and increases the damping, for increasing strain  
152 levels, for one-component shaking, as evidenced by the shear modulus decay curve and damping  
153 ratio curve of the material, given by laboratory tests or inversion techniques (Assimaki *et al.*,  
154 2011). The nonlinear shear stress-strain curve  $(\tau, \gamma)$  during a one-component monotonic loading  
155 is referred to as a backbone curve  $\tau = G(\gamma)\gamma$ , obtained knowing the shear modulus decay curve  
156  $G(\gamma)$ . The backbone curve is assumed, in the present study, adequately described by a  
157 hyperbolic function (Hardin & Drnevich 1972) as

$$158 \quad \tau(\gamma) = G(\gamma)\gamma = \left[ G_0 / (1 + |\gamma/\gamma_r|) \right] \gamma \quad (1)$$

159 however, the MPII constitutive model does not depend on the applied shear modulus decay  
160 curve. It could also incorporate curves obtained from laboratory dynamic tests, as resonant

161 column test (Semblat & Pecker, 2009), on soil samples. The reference shear strain  $\gamma_r$ ,  
162 corresponds to an actual tangent shear modulus equivalent to 50% of the initial shear modulus  
163  $G_0$ . Nonlinear shear stress-strain curve is modelled using a series of mechanical elements,  
164 having different stiffness and increasing sliding resistance. Iwan (1967) modifies the 1D multi-  
165 linear plasticity mechanism  $\tau_k = G_k(\gamma_k, \gamma_{k-1}, \tau_{k-1})\gamma_k$ , where  $G_k = (\tau_k - \tau_{k-1})/(\gamma_k - \gamma_{k-1})$  at each  
166 step  $k$ , by introducing a yield surface in the stress space. The MPII model is a multi-surface  
167 elasto-plastic mechanism with hardening, that takes into account the nonlinear hysteretic  
168 behavior of soils in a three-dimensional stress state, based on the definition of a series of nested  
169 yield surfaces, according to von Mises' criterion. The stress level depends on the strain  
170 increment and strain history but not on the strain rate. Therefore, the energy dissipation process  
171 is purely hysteretic, without viscous damping.

172 The implementation of the MPII nonlinear cyclic constitutive model in the proposed finite  
173 element scheme is presented in detail by Santisi d'Avila *et al.* (2012).

174 The MPII hysteretic model is applied in the present research for dry soils in a three-dimensional  
175 stress state under cyclic loading, allowing a multiaxial total stress analysis. The material strength  
176 is lower under triaxial loading rather than for simple shear loading. From one to three  
177 components unidirectional propagating wave, the shear modulus decreases and the dissipation  
178 increases, for a given maximum strain amplitude.

179 Strains are in the range of stable nonlinearity, where, for one-component loading, both shear  
180 modulus and damping ratio do not depend on the number of cycles and the shape of hysteresis  
181 loops remains unvaried at each cycle. In the case of three-component loading, the shape of the  
182 hysteresis loops changes at each cycle for shear strains in the same range. According to Santisi *et*  
183 *al.* (2012), hysteresis loops for each horizontal direction are altered as a consequence of the

184 interaction between loading components.

185 Large strain rates and liquefaction phenomena are not adequately reproduced without taking into  
186 account pore pressure effects. Constitutive behavior models for saturated soils should allow to  
187 reach larger strains with proper accuracy in future 1D-3C formulations (Viet Anh *et al.*, 2013).

188

## 189 **2.2 Spatial discretization**

190 The stratified soil is discretized into a system of horizontal layers, parallel to the  $xy$  plane, by  
191 using a finite element scheme (Fig. 1), including quadratic line elements with three nodes.

192 According to the finite element modeling, the discrete form of equilibrium equations, is  
193 expressed in the matrix form as

$$194 \quad \mathbf{M} \ddot{\mathbf{D}} + \mathbf{F}_{\text{int}} = \mathbf{0} \quad (2)$$

195 where  $\mathbf{M}$  is the mass matrix,  $\ddot{\mathbf{D}}$  is the acceleration vector that is the second time derivative of  
196 the displacement vector  $\mathbf{D}$ .  $\mathbf{F}_{\text{int}}$  is the vector of nodal internal forces. A non-zero load vector and  
197 damping matrix appear in Santisi d'Avila *et al.* (2012, 2013) where an absorbing boundary  
198 condition is assumed. In this research, there are no damping terms in the equilibrium problem,  
199 because the boundary condition is an imposed motion, downhole records being considered. Figure 1

200 The differential equilibrium problem (2) is solved according to compatibility conditions, the  
201 hypothesis of no strain variation in the horizontal directions, a three-dimensional nonlinear  
202 constitutive relation for cyclic loading and the boundary conditions described below. The Finite  
203 Element Method, as applied in the present research, is completely described in the works of  
204 Batoz & Dhatt (1990), Reddy (1993) and Cook *et al.* (2002).

205 Discretizing the soil column into  $n_e$  quadratic line elements and consequently into  $n = 2n_e + 1$   
206 nodes (Fig. 1), having three translational degrees of freedom each, yields a  $3n$ -dimensional

207 displacement vector  $\mathbf{D}$  composed by three blocks whose terms are the displacements of the  $n$   
 208 nodes in  $x$ -,  $y$ - and  $z$ -direction, respectively. Soil properties are assumed constant in each  
 209 finite element and soil layer.

210 Mass matrix  $\mathbf{M}$  and the vector of internal forces  $\mathbf{F}_{\text{int}}$  are presented in the Appendix.

211 The assemblage of  $(3n \times 3n)$ -dimensional matrices and  $3n$ -dimensional vectors is independently  
 212 done for each of the three  $(n \times n)$ -dimensional submatrices and  $n$ -dimensional subvectors,  
 213 respectively, corresponding to  $x$ -,  $y$ - and  $z$ -direction of motion.

214 The distance between nodes in the three-node line finite element scheme is  $H_j / (2n_e^j)$ , where  
 215  $n_e^j$  is the number of elements in the layer  $j$  having the thickness  $H_j$  (Fig. 1). It is assumed not  
 216 higher than  $d_{\text{max}} = 1\text{ m}$  ( $< 1.5\text{ m}$  for thick rock layers). The minimum number of nodes per  
 217 wavelength  $r$  is such as  $\lambda/r \leq d_{\text{max}}$ . This implies that  $r \geq \lambda/d_{\text{max}}$ . The seismic signal wavelength  
 218  $\lambda$  is equal to  $v_s/f$ , where  $f$  is the assumed maximum frequency of the input signal and  $v_s$  is  
 219 the assumed minimum shear velocity in the medium.

220

### 221 **2.3 Time discretization**

222 The finite element model and the soil nonlinearity require spatial and time discretization,  
 223 respectively, to permit the problem solution (Hughes 1987; Crisfield 1991). The rate type  
 224 constitutive relation between stress and strain is linearized at each time step. Accordingly,  
 225 equation (2) is expressed as

$$226 \quad \mathbf{M} \Delta \mathbf{B}_k^{\otimes} + \mathbf{K}_k^i \Delta \mathbf{D}_k^i = \mathbf{0} \quad (3)$$

227 where the subscript  $k$  indicates the time step  $t_k$  and  $i$  the iteration of the problem solving

228 process, as explained below. The stiffness matrix  $\mathbf{K}_k^i$  is presented in the Appendix.

229 The step-by-step process is solved by the Newmark's algorithm that is an implicit self-starting  
 230 unconditionally stable approach for one-step time integration in dynamic problems (Newmark  
 231 1959; Hilber *et al.* 1977; Hughes 1987). According to Newmark's procedure, the displacement  
 232 variation is expressed as follows:

$$233 \quad \Delta \mathbf{D}_k^i = \Delta t \mathbf{D}_{k-1}^{\otimes} + \frac{\Delta t^2}{2} \mathbf{D}_{k-1}^{\otimes\otimes} + \beta \Delta t^2 \Delta \mathbf{D}_k^{\otimes\otimes} \quad (4)$$

234 Equations (3) and (4) yield

$$235 \quad \bar{\mathbf{M}}_k^i \Delta \mathbf{D}_k^{\otimes\otimes} = \mathbf{A}_k^i \quad (5)$$

236 where the modified mass matrix is defined as

$$237 \quad \bar{\mathbf{M}}_k^i = \mathbf{M} + \beta \Delta t^2 \mathbf{K}_k^i \quad (6)$$

238 and  $\mathbf{A}_k^i$  is a vector depending on the motion at the previous time step, given by

$$239 \quad \mathbf{A}_k^i = -\left(\Delta t \mathbf{K}_k^i\right) \mathbf{D}_{k-1}^{\otimes} - \left(\frac{\Delta t^2}{2} \mathbf{K}_k^i\right) \mathbf{D}_{k-1}^{\otimes\otimes} \quad (7)$$

240 Equation (5) requires an iterative solving, at each time step  $k$ , to correct the tangent stiffness  
 241 matrix  $\mathbf{K}_k^i$ . Starting from the stiffness matrix  $\mathbf{K}_k^1 = \mathbf{K}_{k-1}$ , evaluated at the previous time step, the  
 242 value of matrix  $\mathbf{K}_k^i$  is updated at each iteration  $i$  (Crisfield 1991). An elastic behavior is  
 243 assumed for the first iteration at the first time step.

244 Three terms in the vector of acceleration increments  $\Delta \mathbf{D}_k^{\otimes\otimes}$  are known, that is, the first term of  
 245 each of three  $n$ -dimensional subvectors corresponds to the imposed borehole acceleration at  
 246 node 1 in  $x$ -,  $y$ - and  $z$ -direction of motion. Organizing rows and columns of equation (5) to  
 247 separately group borehole and unknowns parameters of motion (index b and u, respectively),

248 according to

$$249 \quad \begin{bmatrix} \bar{\mathbf{M}}_{bb} & \bar{\mathbf{M}}_{bu} \\ \bar{\mathbf{M}}_{ub} & \bar{\mathbf{M}}_{uu} \end{bmatrix}_k^i \begin{bmatrix} \Delta \mathbf{D}_b^{\otimes} \\ \Delta \mathbf{D}_u^{\otimes} \end{bmatrix}_k^i = \begin{bmatrix} \mathbf{A}_b \\ \mathbf{A}_u \end{bmatrix}_k^i \quad (8)$$

250 the unknown acceleration increments are evaluated consequently, as

$$251 \quad \left[ \Delta \mathbf{D}_u^{\otimes} \right]_k^i = \left[ \bar{\mathbf{M}}_{uu}^{-1} \right]_k^i \left( \left[ \mathbf{A}_u \right]_k^i - \left[ \bar{\mathbf{M}}_{ub} \right]_k^i \left[ \Delta \mathbf{D}_b^{\otimes} \right]_k^i \right) \quad (9)$$

252 After evaluating the unknown acceleration increment  $\left[ \Delta \mathbf{D}_u^{\otimes} \right]_k^i$ , at all nodes except the first one,

253 by equation (9), using the tangent stiffness matrix corresponding to the current time step, and

254 then the acceleration increment vector  $\Delta \mathbf{D}_k^{\otimes}$ , the total motion is obtained according to Newmark's

255 procedure as

$$256 \quad \begin{cases} \mathbf{D}_k^{\otimes} = \mathbf{D}_{k-1}^{\otimes} + \Delta \mathbf{D}_k^{\otimes} \\ \mathbf{D}_k^{\dot{\otimes}} = \left( \mathbf{D}_{k-1}^{\dot{\otimes}} + \Delta t (1 - \alpha) \mathbf{D}_{k-1}^{\ddot{\otimes}} \right) + \alpha \Delta t \mathbf{D}_k^{\ddot{\otimes}} \\ \mathbf{D}_k^i = \left( \mathbf{D}_{k-1}^i + \Delta t \mathbf{D}_{k-1}^{\dot{\otimes}} + \frac{\Delta t^2}{2} (1 - 2\beta) \mathbf{D}_{k-1}^{\ddot{\otimes}} \right) + \beta \Delta t^2 \mathbf{D}_k^{\ddot{\otimes}} \end{cases} \quad (10)$$

257 where  $\mathbf{D}_k^i$ ,  $\mathbf{D}_k^{\dot{\otimes}}$  and  $\mathbf{D}_k^{\ddot{\otimes}}$  are the vectors of total displacement, velocity and acceleration,

258 respectively. The two parameters  $\beta = 0.3025$  and  $\alpha = 0.6$  guarantee unconditional stability of

259 the time integration scheme and numerical damping properties to damp higher modes (Hughes

260 1987).

261 The strain increments are then derived from the displacement increments  $\mathbf{D}_k^i - \mathbf{D}_{k-1}^i$ . Stress

262 increments and tangent constitutive matrix are obtained through the assumed constitutive

263 relationship. Gravity load is imposed as static initial condition in terms of strain and stress at

264 nodes. The stiffness matrix  $\mathbf{K}_k^i$  and the modified mass matrix  $\bar{\mathbf{M}}_k^i$  are then calculated and the

265 process restarts. The correction process continues until the difference between two successive  
266 approximations is reduced to a fixed tolerance, according to

$$267 \quad \left| \mathbf{D}_k^i - \mathbf{D}_k^{i-1} \right| < \eta \left| \mathbf{D}_k^i \right| \quad (11)$$

268 where  $\eta = 10^{-3}$  (Mestat 1993, 1998). Afterwards, the next time step is analyzed.

269

## 270 **2.4 Boundary conditions**

271 The system of horizontal soil layers is bounded at the top by the free surface and the stresses  
272 normal to it are assumed null.

273 The largely adopted absorbing boundary condition at the soil-bedrock interface, proposed by  
274 Joyner & Chen (1975), is used in a 1D-3C wave propagation model by Santisi d'Avila *et al.*  
275 (2012, 2013). Some rock type profiles are selected close to each analyzed soil column and the  
276 halved signal recorded at these rock outcrops are applied as 3C incident wave. Computed and  
277 recorded motions at the surface of analyzed soil profile are compared to validate the 1D-3C  
278 model. A great variability of the seismic response is observed at the surface of soil profiles, with  
279 the selected bedrock motion. The accuracy of the predicted soil motion depends significantly on  
280 the rock motion characteristics. The lack of geotechnical data could induce to questionable  
281 results when the geological homogeneity of selected rock type outcrops and the modeled  
282 bedrock, underlying analyzed soil profiles, is not assessed.

283 When borehole records are used, the motion at the soil-bedrock interface (node 1 in Fig. 1),  
284 containing incident and reflected waves, is known and directly imposed as boundary condition.

285 The soil and quake properties are related to the same stratigraphy, increasing the accuracy of  
286 results. Borehole records are imposed in terms of three-component accelerations at node 1 of the  
287 finite element scheme.

288

### 289 **3 SOIL PROPERTIES AND QUAKE FEATURES**

290 Recorded data from the 11 March 2011 Mw 9 Tohoku earthquake stored by the Kiban-Kyoshin  
291 Network (KiK-Net) accelerometer network have been analyzed in this research, to numerically  
292 reproduce the ground motion at the surface and to provide profiles with depth of mechanical and  
293 motion parameters. The KiK-Net database stores surface and borehole seismic records for  
294 different stratigraphies.

295 Records at the surface of some selected alluvial soil profiles (Fig. 2) are used to validate the  
296 numerical surface ground motion computed by the proposed 1D-3C model, by using the borehole  
297 records as inputs, imposed as boundary condition at the base of the soil profiles. The validation is  
298 done using records at the ground surface, since it is the only available motion record.

Figure 2

299

#### 300 **3.1 Soil profiles**

301 The stratigraphic setting of four soil profiles in the Tohoku area (Japan) is used in this analysis  
302 (Fig. 2). The description of the stratigraphy and lithology of these alluvial deposits is provided  
303 by the KiK-Net database. Epicentral distances are listed in Table 1. Analyzed profiles have been  
304 selected between stratigraphies proposed by KiK-Net, adopting as criteria the choice of soil type  
305 profiles and a high vertical to horizontal component ratio of the ground motion measured at their  
306 surface. Soil profiles have different properties: depth  $H$ , number and thickness of layers  $N$ ,  
307 average shear wave velocity  $v_s = H / \sum_{j=1}^N H_j / v_{s,j}$ , soil type and seismic velocity ratio  
308 (compressional to shear wave velocity ratio  $v_p / v_s$ ) that is related to the Poisson's ratio (Table 1).  
309 Stratigraphies used in this analysis and soil properties of each layer  $j$ , as thickness  $H_j$ , shear and  
310 pressure wave velocity in the medium, density  $\rho$  and the reference shear strain  $\gamma_r$ , are shown in

311 Tables 2-5. Soil properties are assumed homogeneous in each layer. Table 1

312 The nonlinear mechanical properties of the Tohoku alluvial deposits are not provided. The  
313 normalized shear modulus decay curves employed in this work are obtained according to the  
314 hyperbolic model. The applied reference shear strain  $\gamma_r$  corresponds, for each soil type in the  
315 analyzed profiles, to an actual tangent shear modulus equivalent to 50 % of the initial shear  
316 modulus, in a normalized shear modulus decay curves of the literature (Tables 2-5). Curves  
317 proposed by Seed & Idriss (1970) are used to define the reference strain for sands and the curve  
318 of Seed & Sun (1989) is applied for clays. A plasticity index in the range of  $PI = 5 - 10$  is  
319 assumed in the relationship of Sun *et al.* (1988) to define the reference strain for silt. The  
320 reference shear strain for gravel is defined according to Seed *et al.* (1986). An almost linear  
321 behavior is assumed for stiff layers ( $\gamma_r = 100 \%$ ).

322 The density of soil layers is not even provided by the KiK-Net database, consequently it is  
323 assumed, based on density range for each soil type.

Tables 2, 3, 4, 5

324

### 325 **3.2 Seismic excitations**

326 The 2011 Tohoku earthquake is one of the largest earthquakes in the world that has been well  
327 recorded in the near-fault zone. The vertical to maximum horizontal component ratio appears  
328 close to one for several soil profiles and the peak vertical motion can locally be higher than the  
329 minor horizontal component of ground motion. The four analyzed soil profiles have been  
330 selected because having a high vertical to horizontal peak ground acceleration ratio (Table 1)  
331 during the 11 March 2011 Mw 9 Tohoku earthquake. The peak ground acceleration (PGA)  
332 recorded at the surface of analyzed soil profiles is higher than the acceleration level commonly  
333 used for structural design in high risk seismic zones. The three components of motion are

334 recorded in North-South (NS), East-West (EW) and Up-Down (UP) directions, respectively  
335 referred to as  $x$ ,  $y$  and  $z$  in the proposed model. Recorded signals have different polarizations.  
336 The three maximum acceleration components, in each direction of motion, correspond to  
337 different time instants. Peaks of the three components of motion at the base and surface of  
338 analyzed soil profiles are synthetized in Tables 6 and 7, respectively. The waveforms are  
339 provided by the KiK-Net strong ground motion database. Borehole seismic records are measured  
340 at various depths (Table 1). Table 6, 7

341 Three-component seismic signals recorded downhole in directions NS, EW and UD, during the  
342 2011 Tohoku earthquake (Table 6), are propagated in the various soil columns. The three  
343 components induce shear loading in horizontal directions  $x$  (NS) and  $y$  (EW) and pressure  
344 loading in  $z$ -direction (UD).

345 Downhole and surface recorded time histories, in terms of acceleration modulus, are compared  
346 in Fig. 3 to show the strong amplification effects in these alluvial deposits. Vertical to maximum  
347 horizontal component ratios are indicated in Table 1. Figure 3

348 In this research, the maximum frequency is imposed as  $f = 10$  Hz and the minimum shear  
349 velocity in the soil  $v_s$  is 150 m/s (Table 2) then, the minimum number of nodes per wavelength  
350  $r$  is always higher than 10 in all the analyzed cases, to accurately represent the seismic signal.

351

#### 352 **4 1D-3C LOCAL SEISMIC RESPONSE ANALYSIS OF THE TOHOKU AREA**

353 The local dynamic response of analyzed soil profiles to the one-directional seismic wave  
354 propagation is presented, validated and discussed.

355

356

#### 357 **4.1 Validation of the 1D-3C model by GoF criteria**

358 Numerical acceleration and velocity time histories appear consistent with recordings in Figs 4-7.  
359 Nevertheless, the goodness of synthetic seismograms must be confirmed by comparing  
360 statistical characteristics.

361 The validation of the proposed model and numerical procedure is done by comparison of  
362 computed results with records using Anderson's Goodness of Fit (GoF) criteria (Anderson  
363 2004). Quantitative scores proposed by Anderson are estimated to characterize the GoF of 1D-  
364 3C synthetics. According to him, the agreement between records and numerical results are  
365 classified as poor fit if the score is below 4 over 10, fair fit in the range 4/10 - 6/10, good fit for  
366 6/10 - 8/10 and excellent fit for scores higher than 8 over 10. The error is measured as follows:

$$367 \quad S(p_n, p_r) = 10 \exp \left[ - \left( \frac{p_n - p_r}{\min(p_n, p_r)} \right)^2 \right] \quad (12)$$

368 where  $p_n$  and  $p_r$  are evaluated parameters for numerical seismograms and records,  
369 respectively. Records and numerical signals shown in following figures are band-pass filtered  
370 between 0.05 and 10 Hz. The whole band of frequency is analyzed in the comparisons.

371 The seismograms are adequately fitted in terms of peak acceleration and peak velocity that are  
372 listed in Table 7, for the three components of motion at the surface of the four analyzed soil  
373 profiles. Bold characters indicate measured PGA. Records are band-pass filtered in the same  
374 frequency band as synthetics to allow comparisons. Signals in Fig. 4 (MYGH09) show excellent  
375 fit (over 9) for horizontal components, in terms of acceleration, and a good fit for the vertical  
376 component. Velocities provide an excellent fit for the three components. Synthetics in Fig. 5  
377 (FKSH20) show an excellent fit of  $x$ -component and poor and fair fit for  $y$ - and  $z$ -component,  
378 respectively. Instead,  $x$ - and  $z$ -velocities are excellently fitted and  $y$ -velocity is well fitted.

379 Seismograms in Fig. 6 (IWTH04) show clearly an excellent fit for horizontal accelerations and  
380 velocities and a fair and poor fit for  $z$ -direction, in terms of velocity and acceleration,  
381 respectively. Records at the surface of soil profile IBRH12 (Fig. 7) obtain excellent and good  
382 scores for horizontal accelerations and three components of velocity and a fair score for vertical  
383 acceleration. Comparing the peak displacement of seismograms, we obtain a great variability of  
384 scores. Grades for peak acceleration (PA), peak velocity (PV) and peak displacement (PD) are  
385 evaluated according to Anderson's criterion (12) and listed in Table 8.

Figures 4, 5, 6, 7

386 A comparison of peaks is incomplete to guarantee the GoF of synthetic seismograms. Analyzing  
387 other parameters suggested by Anderson (2004), like the shape of the normalized integrals of  
388 acceleration and velocity squared, normalized with respect to Arias intensity and the energy  
389 integral respectively, we observe excellent fit for MYGH09 (Fig. 8), good and excellent fit for  
390 various components at the surface of FKSH20, IWTH04 and IBRH12 profiles (see NIA and NIE  
391 columns in Table 8). The energy integral is the integral of velocity squared for the complete  
392 duration of the accelerogram.

393 Verifying the values used for normalization, that are the Arias intensity (IA) and the energy  
394 integral (IE), the error reaches different scores (Table 8). The scores confirm the differences  
395 remarked in acceleration and velocity time histories. Fitting of  $z$ -component is often the most  
396 difficult. See for example the case of IWTH04 profile (Fig. 6), with vertical to horizontal  
397 component ratio greater than 1. This raises the question of whether compressive behavior is  
398 properly modeled when a multiaxial loading is applied with a high pressure component.

Figure 8

399 Finally, we observed acceleration response and Fourier spectra. A 5% damping is assumed to  
400 derive the acceleration response spectrum. According to Anderson (2004), the score related to  
401 the Fourier spectrum and the cross-correlation in the whole band of frequency are lower than

402 others (see FFT and CC columns in Table 8). A poor fit is obtained in all cases. Instead, an  
403 excellent fit is attained, in terms of acceleration response spectrum, for the maximum horizontal  
404 and vertical components in MYGH09, the  $x$ -component in FKSH20, both horizontal  
405 components in IWTH04 and the  $y$ -component in IBRH12. Fair fits are obtained in other cases  
406 (see SA column in Table 8). Best fitted spectra, for each soil profile, are reproduced in Fig. 9,  
407 where seismic response amplification from the bottom to the surface can be observed in terms of  
408 acceleration response spectrum.

Figure 9

409 The lack of data about soil properties, such as density and  $G(\gamma)$ , demands future studies to  
410 analyze if the results could be improved when all measurable data are available. The choice of  
411 density and shear modulus decay curve, for each soil layer, strongly influence the analysis,  
412 modifying, respectively, the initial elastic properties and material behavior at larger strains.  
413 Furthermore, amplification effects at the surface of soil profiles and energy spectra are modified  
414 not only by soil properties of each individual layer, but especially by the combination of seismic  
415 impedances of various soil layers. Soil profile layering complicating the issue, measured soil  
416 properties used for all input data in the numerical model would lead to more reliable results. In  
417 particular when various layers are modeled (12 layers in MYGH09, 28 in IBRH12), a great  
418 variability of results can be obtained with different assumptions for density and reference shear  
419 strain of each layer. The benchmark Prenolin, as part of Cashima research project, will provide  
420 measured soil and quake data for some study cases and will allow to adjust 1D seismic wave  
421 propagation models.

Table 8

422

#### 423 **4.2 Local dynamic response of soil profiles**

424 The proposed model allows to study the local seismic response in case of strong earthquakes

425 affecting alluvial sites and assess possible amplifications of seismic motion at the surface,  
426 influenced by stratigraphic characteristics. Non-measured parameters of motion, stress and strain  
427 along the soil profiles can be computed, in order to investigate nonlinear effects in deeper details.  
428 Modeling the one-directional propagation of a three-component earthquake allows to take into  
429 account the interactions between shear and pressure components of the seismic load. Nonlinear  
430 and multiaxial coupling effects appear under a triaxial stress state induced by a cyclic 3D  
431 loading. The interaction between multiaxial stresses in the 3C approach allows to reproduce  
432 energy dissipation effects that yields a reduction of the ground motion at the surface, compared  
433 with the approach considering the superposition of three one-component propagations.

434

#### 435 *4.2.1 Response with depth*

436 The seismic response of soil profiles MYGH09, FKSH20, IWTH04 and IBRH12, to the  
437 propagation of a three-component signal (1D-3C approach), is analyzed in terms of depth  
438 profiles of maximum acceleration and velocity of each component of motion and maximum  
439 shear stress and strain and in terms of shear stress-strain loops in the most deformed layer (Figs  
440 10-13). Stratigraphies and soil properties are given in Tables 2-5. The profile of maximum  
441 motion vs depth shows, at each  $z$ -coordinate, the peak of the ground motion during shaking. The  
442 same criterion is adopted for strain and stress profiles. The maximum acceleration profiles with  
443 depth are displayed in all these figures without low-pass filtering operations.

444 Parameters of motion, stress and strain along the analyzed soil profiles, evaluated by the 1D-3C  
445 approach, are influenced by the input motion polarization and 3D loading path. Both shear  
446 stresses,  $\tau_{yz}$  and  $\tau_{zx}$ , and non-zero normal stress components  $\sigma_{xx}$ ,  $\sigma_{yy}$  and  $\sigma_{zz}$  are assessed  
447 along the soil profile, consequence of the three strains in  $z$ -direction,  $\gamma_{yz}$ ,  $\gamma_{yz}$  and  $\varepsilon_{zz}$ .

448 Soft layers and high strain jumps at layer interfaces can be identified evaluating the maximum  
449 strain profiles with depth. We observe that maximum strains along the soil profile are located at  
450 layer interfaces (Figs 10a, 11a, 12a and 13).

451 The wave polarization is modified along the depth. The PGA does not correspond to the same  
452 horizontal component all along the soil profile. Since polarization changes along the depth, at a  
453 given depth, nonlinear effects and strain level are more important for the maximum peak  
454 horizontal component at this depth and not for the direction of measured PGA at the ground  
455 surface (see hysteresis loop for the minimum horizontal component at the surface in Figs 10 and  
456 12).

Figures 10, 11, 12, 13

#### 458 4.2.2 Hysteresis loops

459 Cyclic shear strains with amplitude higher than the elastic behavior range limit give open loops  
460 in the shear stress-shear strain plane, exhibiting strong hysteresis. Due to nonlinear effects, the  
461 shear modulus decreases and the dissipation increases with increasing strain amplitude. In the  
462 case of one-component loading, the shape of the first loading curve is the same as the backbone  
463 curve and the shape of hysteresis loops remains unvaried at each cycle, for shear strains in the  
464 range of stable nonlinearity (Santisi d'Avila *et al.* 2012). In the case of three-component loading,  
465 the shape of the hysteresis loops changes at each cycle, even in a strain range corresponding to  
466 stable nonlinearity in the 1C case. The shape of the loops is indeed disturbed by the multiaxial  
467 stress coupling. Under triaxial loading the material strength is lower than for simple shear  
468 loading, referred to as the backbone curve. The cyclic response of the soil column in terms of  
469 shear stress and strain, when it is excited by a triaxial input signal (1D-3C), is shown in Figs 10b-  
470 12b. The shape of the shear stress-strain cycles in  $x$ -direction (respectively  $y$ -direction) reflects

471 the coupling effects with loads in directions  $y$  (respectively  $x$ ) and  $z$ . Hysteresis loops for each  
472 horizontal direction are altered as a consequence of the interaction between loading components.  
473 The strain level reached in the stiff IBRH12 profile is low, with closely linear behavior.  
474 We detect, in all hysteresis loops (Figs 10b-12b), two successive events which is a feature of the  
475 2011 Tohoku earthquake (Bonilla *et al.* 2011). Observing Figs 4-7, these two successive events  
476 can be easily distinguished, confirming the reliability of the proposed model.

477

#### 478 4.2.3 Component ratio vs time

479 Fig. 14 shows the seismic wave polarization with time, at the surface of the analyzed soil  
480 profiles, in terms of acceleration. The 3D polarization is represented by a unit vector, whose  
481 components are  $\bar{a}_x$ ,  $\bar{a}_y$  and  $\bar{a}_z$ , with respect to  $x$ -,  $y$ - and  $z$ -axis respectively. Acceleration  
482 parameters  $\bar{a}_x = a_x/|a|$ ,  $\bar{a}_y = a_y/|a|$  and  $\bar{a}_z = a_z/|a|$  are the normalized acceleration components  
483 with respect to acceleration modulus  $|a|$ . The three shares  $(\bar{a}_x^2 / \sqrt{\bar{a}_x^2 + \bar{a}_y^2}) \cos \alpha$ ,  
484  $(\bar{a}_y^2 / \sqrt{\bar{a}_x^2 + \bar{a}_y^2}) \cos \alpha$  and  $|\bar{a}_z| \sin \alpha$  are the projections of the three normalized acceleration  
485 components  $\bar{a}_x$ ,  $\bar{a}_y$  and  $\bar{a}_z$ , respectively, in the wave propagation direction (the direction of the  
486 unit vector), as a consequence their sum is equal to one. The angle  $\theta$ , such as  
487  $\tan \theta = |\bar{a}_z| / \sqrt{\bar{a}_x^2 + \bar{a}_y^2}$ , is the projection angle of the unit vector in  $xy$  horizontal plane. The  
488 representation of normalized acceleration contribution for the three components of motion,  
489 during the total duration of numerical and recorded seismograms, is shown in Fig. 14.

Figure 14

490 The variability of the contribution of each component of motion with time is an interesting result,  
491 to assess the reliability of the proposed 1D-3C model. The direction of the PGA (Max SH in Fig.

492 14) does not correspond to the maximum acceleration direction all along the signal duration.  
493 The direction of maximum horizontal component of motion changing with time, as well as the  
494 importance of the vertical component (P in Fig. 14), confirm the interest of taking into account  
495 the three-component coupling in 1D wave propagation models. Unsteady results are obtained for  
496 very low acceleration rates at the earthquake starting. This could be justified by the fact that the  
497 constitutive soil model is not calibrated for very small strain levels.

498

## 499 **5 CONCLUSIONS**

500 A one-dimensional three-component (1D-3C) approach, allowing to analyze the propagation  
501 along 1D soil profiles of 3C seismic waves, recorded downhole, is proposed, validated and  
502 discussed.

503 A three-dimensional constitutive relation of the Masing-Prandtl-Ishlinskii-Iwan (MPII) type, for  
504 cyclic loading, is implemented in a finite element scheme, modeling a horizontally multilayered  
505 soil. This constitutive model has been selected because emulating a 3D behavior, nonlinear for  
506 both loading and unloading, and, above all, because few parameters are necessary to characterize  
507 the soil hysteretic behavior.

508 Borehole records from 2011 Tohoku earthquake are used as 3C seismic excitations, imposed as a  
509 boundary condition at the base of the stacked horizontal soil layers.

510 The influence of the quake features and site-specific seismic hazard can be investigated by such  
511 a model. The soil and quake properties being associated to the same soil profile allows to  
512 perform quantitative analyses with acceptable accuracy.

513 The validation of the 1D-3C approach from recorded time histories is presented in this paper for  
514 four soil profiles in the Tohoku area (Japan), shaken by the 11 March 2011 Mw 9 Tohoku

515 earthquake. Anderson's criteria are applied to assess the reliability of numerical seismograms.  
516 Synthetics adequately reproduce the records. In particular for the 2011 Tohoku earthquake, the  
517 two successive events, detected by records, are numerically replicated. The lack of measured  
518 data justifies the assumption of some soil properties (density and shear modulus decay curve)  
519 according to the literature. This demands future studies, to analyze if results are improved in  
520 cases where all measurable data are available.

521 The effects of the input motion polarization and 3D loading path can be detected by the 1D-3C  
522 approach. It allows to evaluate non-measured parameters of motion, stress and strain along the  
523 analyzed soil profiles, in order to detail nonlinear effects and the influence of soil profile layering  
524 on local seismic response. Maximum strains are induced at layer interfaces, where waves  
525 encounter large variations of impedance contrast, along the soil profile.

526 The wave polarization is modified along the propagation path. The PGA does not correspond to  
527 the same horizontal component all along the soil profile. For this reason, at a given depth,  
528 nonlinear effects and strain level are more important for the maximum peak horizontal  
529 component at this depth and not for the direction of measured PGA at the ground surface.

530 A low seismic velocity ratio in the soil and a high vertical to horizontal component ratio increase  
531 the three-dimensional mechanical interaction and progressively change the hysteresis loop size  
532 and shape at each cycle, even in a strain range of stable nonlinearity in the 1C case.

533 The variability of the propagating wave polarization with time and the significant contribution of  
534 vertical component confirm the importance of taking into account the three component coupling  
535 in 1D wave propagation models.

536 The extension of this approach to higher strain rates, considering the consequences of soil  
537 nonlinearity in saturated conditions, would be a natural improvement of the proposed 1D-3C

538 model.

539 Statistical studies using records of different earthquakes at a same site could be undertaken using  
540 the 1D-3C approach, for the evaluation of local seismic response for site effect analyses.

541

## 542 **ACKNOWLEDGMENTS**

543 Seismograms and soil stratigraphic setting used in this study are provided by the National  
544 research Institute for Earth science and Disaster prevention (NIED), in Japan, and can be  
545 obtained from the Kiban-Kyoshin Network at [www.k-net.bosai.go.jp](http://www.k-net.bosai.go.jp) (last accessed January  
546 2013).

547 We thank Mario Ordaz for providing Degtra software, developed by the Universidad National  
548 Autonoma de Mexico.

549

## 550 **REFERENCES**

551 Anderson, J.G., 2004. Quantitative measure of the goodness-of-fit of synthetic seismograms,  
552 *13th World Conference on Earthquake Engineering*, Paper no. 243, Vancouver, Canada.

553 Assimaki, D., Li W. & Kalos A., 2011. A wavelet-based seismogram inversion algorithm for the  
554 in situ characterization, *Pure Appl. Geophys.*, 168, 1669–1691.

555 of Nonlinear Soil Behavior

556 Bard, P.Y. & Bouchon E.T., 1985. Underground and ridge site effects: a comparison of  
557 observation and theory, *Bull. Seism. Soc. Am.*, 75, 905–922.

558 Bardet, J.P., Ichii K., & Lin C.H., 2000. *EERA: A computer program for Equivalent-linear*  
559 *Earthquake site Response Analyses of layered soil deposits*, University of Southern California,

560 United States.

561 Bardet, J.P. & Tobita T., 2001. *NERA: A computer program for Nonlinear Earthquake site*  
562 *Response Analyses of layered soil deposits*, University of Southern California, United States.

563 Batoz J.L. & Dhatt G., 1990. *Modélisation des structures par éléments finis*, Vol. 1, Hermes,  
564 Paris, France.

565 Bertotti, G. & Mayergoyz I., 2006. *The science of hysteresis: mathematical modeling and*  
566 *applications*, Elsevier, Amsterdam, Netherlands, 1–114.

567 Bonilla, L.F., Tsuda K., Pulido N., Régnier J., & Laurendeau A., 2011. Nonlinear site response  
568 evidence of K-Net and KiK-Net records from the 2011 off the Pacific coast of Tohoku  
569 Earthquake, *Earth Planets Space*, 63, 785–789.

570 Cook R.D., Malkus D.S., Plesha M.E. & Witt R.J., 2002. *Concepts and applications of finite*  
571 *element analysis*, 4th edn, John Wiley & Sons, New York, United States.

572 Crisfield, M.A., 1991. *Non-linear finite element analysis of solids and structures*, Vol. 1, John  
573 Wiley and Sons, Chichester, England, 8–55.

574 Delépine, N., Bonnet G., Lenti L. & Semblat J.F., 2009. Nonlinear viscoelastic wave  
575 propagation: an extension of Nearly Constant Attenuation models, *J. Eng. Mech.*, 135(11),  
576 1305–1314.

577 Hardin, B.O., & Drnevich V.P., 1972. Shear modulus and damping in soil: design equations and  
578 curves, *J. Soil Mech. Found. Div.*, 98, 667–692.

579 Hashash Y.M.A. & Park D., 2001. Non-linear one-dimensional seismic ground motion  
580 propagation in the Mississippi embayment, *Eng. Geology*, 62(1–3), 185–206.

581 Hilber, H.M., Hughes T.J.R., & Taylor R.L., 1977. Improved numerical dissipation for time  
582 integration algorithms in structural dynamics, *Earthquake Eng. Struct. Dyn.*, 5, 283–292.

583 Hughes, T.J.R., 1987. *The finite element method - Linear static and dynamic finite element*  
584 *analysis*, Prentice Hall, Englewood Cliffs, New Jersey, 490–567.

585 Iwan, W.D., 1967. On a class of models for the yielding behavior of continuous and composite  
586 systems, *J. Appl. Mech.*, 34, 612–617.

587 Joyner, W., 1975. A method for calculating nonlinear seismic response in two dimensions, *Bull.*  
588 *Seism. Soc. Am.*, 65(5), 1337–1357.

589 Joyner, W.B., & Chen A.T.F., 1975. Calculation of nonlinear ground response in earthquakes,  
590 *Bull. Seism. Soc. Am.*, 65(5), 1315–1336.

591 Kausel, E., & Assimaki, D., 2002. Seismic Simulation of Inelastic Soils via Frequency-  
592 Dependent Moduli and Damping, *J. Eng. Mech.*, 128(1), 34–47.

593 Lee, K.W., & Finn W.D.L., 1978. DESRA-2: Dynamic effective stress response analysis of soil  
594 deposits with energy transmitting boundary including assessment of liquefaction potential, in  
595 *Soil Mechanics Series*, University of British Columbia, Vancouver, Canada.

596 Li, X.S., 1990. *Free field response under multidirectional earthquake loading*, PhD thesis,  
597 University of California, Davis, United States.

598 Li, X.S., Wang Z.L., & Shen C.K., 1992. *SUMDES: A nonlinear procedure for response*  
599 *analysis of horizontally-layered sites subjected to multi-directional earthquake loading*,  
600 University of California, Davis, United States.

601 Matasovic N., 2006. *D-MOD\_2: A Computer Program for Seismic Response Analysis of*  
602 *Horizontally Layered Soil Deposits, Earthfill Dams, and Solid Waste Landfills. User's Manual*,  
603 GeoMotions, LLC, Washington.

604 Mestat, P., 1993. Lois de comportement des géomatériaux et modélisation par la méthode des

605 éléments finis, in *Etudes et recherches des Laboratoires des Ponts et Chaussées*, Geotechnical  
606 Series, GT52, Paris, France.

607 Mestat, P., 1998. Modèles d'éléments finis et problèmes de convergence en comportement non  
608 linéaire, *Bull. Lab. Ponts Chaussées*, 214, 45–60.

609 Newmark, N.M., 1959. A method of computation for structural dynamics. *J. Eng. Mech.*,  
610 85(EM3), 67–94.

611 Oppenheim, A.V., Willsky A.S., & Nawab S.H., 1997. *Signals and systems*, 2nd edn, Prentice  
612 Hall, Upper Saddle River, New Jersey, 53–56.

613 PEERC, 2008. *Benchmarking of nonlinear geotechnical ground response analysis procedures*,  
614 PEER Report 2008/04, University of California, Berkeley, United States.

615 Reddy J. N., 1993. *An introduction to the finite element method*, 2nd edn, Mac Graw Hill,  
616 Hightstown, New Jersey.

617 Santisi d'Avila M.P., Lenti L., & Semblat J.F., 2012. Modeling strong seismic ground motion:  
618 3D loading path vs wavefield polarization, *Geophys. J. Int.*, 190, 1607–1624.

619 Santisi d'Avila M.P., Semblat J.F. & Lenti L., 2013. Strong Ground Motion in the 2011 Tohoku  
620 Earthquake: a 1Directional - 3Component Modeling, *Bull. Seism. Soc. Am.*, Special issue on the  
621 2011 Tohoku Earthquake, 103(2b).

622 Schnabel, P.B., Lysmer J., & Seed H.B., 1972. SHAKE: A computer program for earthquake  
623 response analysis of horizontally layered sites, *Report UCB/EERC-72/12*, Earthquake  
624 Engineering Research Center, University of California, Berkeley, United States.

625 Seed, H.B., & Idriss I.M., 1970. Soil moduli and damping factors for dynamic response  
626 analyses, *Report UCB/EERC-70/10*, Earthquake Engineering Research Center, University of

627 California, Berkeley, United States.

628 Seed, H.B., & Sun J.I., 1989. Implication of site effects in the Mexico City earthquake of  
629 September 19, 1985 for Earthquake-Resistant Design Criteria in the San Francisco Bay Area of  
630 California, *Report UCB/EERC-89/03*, Earthquake Engineering Research Center, University of  
631 California, Berkeley, United States.

632 Seed H.B., Wong R.T., Idriss I.M., & Tokimatsu K., 1986. Moduli and damping factors for  
633 dynamic analyses of cohesionless soils, *Report UCB/EERC-84/14*, Earthquake Engineering  
634 Research Center, University of California, Berkeley, United States.

635 Segalman, D.J., & Starr M.J., 2008. Inversion of Masing models via continuous Iwan systems,  
636 *Int. J. Nonlinear Mech.*, 43, 74–80.

637 Semblat, J.F. & Pecker A., 2009. *Waves and vibrations in soils*, IUSS Press, Pavia, Italy.

638 Sun, J.I., Goleorkhi R., & Seed H.B., 1988. Dynamic moduli and damping ratios for cohesive  
639 soils, *Report UCB/EERC-88/15*, Earthquake Engineering Research Center, University of  
640 California, Berkeley, United States.

641 Viet Anh, P., Lenti L., Bonilla F., Semblat J.F. & Santisi d’Avila M.P., 2013. Réponse sismique  
642 non linéaire des sols et influence de la pression interstitielle, *French Conference on Mechanics*,  
643 Bordeaux, France.

644 Wang, Z.L., Dafalias Y.F., & Shen C.K., 1990. Bounding surface hypoelasticity model for sand,  
645 *J. Eng. Mech.*, 116, 5, 983–1001.

646

647

648

649 **FIGURE LEGENDS**

650 **Figure 1.** Spatial discretization of a horizontally layered soil excited at its base (node 1) by a  
651 three-component borehole seismic record.

652 **Figure 2.** Location of analyzed soil profiles in the Tohoku area (Japan), KiK-Net accelerometers  
653 being placed at the surface and at depth.

654 **Figure 3.** Time history of measured acceleration modulus at the base and surface of soil profiles  
655 MYGH09 (a), IWTH04 (b), FKSH20 (c) and IBRH12 (d), during the 2011 Tohoku earthquake.

656 **Figure 4.** Time history of measured and numerical acceleration (top) and velocity (bottom), in  
657 directions NS (left), EW (middle) and UD (right), at the surface of soil profile MYGH09, during  
658 the 2011 Tohoku earthquake.

659 **Figure 5.** Time history of measured and numerical acceleration (top) and velocity (bottom), in  
660 directions NS (left), EW (middle) and UD (right), at the surface of soil profile FKSH20, during  
661 the 2011 Tohoku earthquake.

662 **Figure 6.** Time history of measured and numerical acceleration (top) and velocity (bottom), in  
663 directions NS (left), EW (middle) and UD (right), at the surface of soil profile IWTH04, during  
664 the 2011 Tohoku earthquake.

665 **Figure 7.** Time history of measured and numerical acceleration (top) and velocity (bottom), in  
666 directions NS (left), EW (middle) and UD (right), at the surface of soil profile IBRH12, during  
667 the 2011 Tohoku earthquake.

668 **Figure 8.** Normalized integral of acceleration (top) and velocity (bottom) squared for soil profile  
669 MYGH09.

670 **Figure 9.** Numerical best fitted spectra, for soil profiles MYGH09 (a), IWTH04 (b), FKSH20 (c)  
671 and IBRH12 (d), and spectra corresponding to records at the bottom and at the surface.

672 **Figure 10.** 1D-3C seismic response of soil profile MYGH09, during the 2011 Tohoku  
673 earthquake, in both horizontal directions of motion: acceleration, velocity, strain and stress with  
674 depth (a); shear stress-strain loops at 2 m depth (b).

675 **Figure 11.** 1D-3C seismic response of soil profile FKSH20, during the 2011 Tohoku earthquake,  
676 in both horizontal directions of motion: acceleration, velocity, strain and stress with depth (a);  
677 shear stress-strain loops at 31 m depth (b).

678 **Figure 12.** 1D-3C seismic response of soil profile IWTH04, during the 2011 Tohoku earthquake,  
679 in both horizontal directions of motion: acceleration, velocity, strain and stress with depth (a);  
680 shear stress-strain loops at 4 m depth (b).

681 **Figure 13.** 1D-3C seismic response of soil profile IBRH12, during the 2011 Tohoku earthquake,  
682 in both horizontal directions of motion: acceleration, velocity, strain and stress with depth.

683 **Figure 14.** Recorded (top) and numerical (bottom) normalized polarization of seismic waves in  
684 terms of acceleration at the surface of soil profiles MYGH09 (a), FKSH20 (b), IWTH04 (c) and  
685 IBRH12 (d). Max SH is the PGA horizontal direction and P is the vertical direction.

686

687

688

689

690

691

692

693

694

695 **TABLES**

696

697 **Table 1.** Selected soil profiles in the Tohoku area (Japan)

Site name - Prefecture	Site code	Epicentral distance (km)	Depth H (m)	Average $v_s$ (m s <sup>-1</sup> )	$a_z$ / PGA (%)	$\min \{v_p / v_s\}$
SHIROISHI - MIYAGIKEN	MYGH09	198	100	560	90	2.42
NAMIE - FUKUSHIMAKEN	FKSH20	178	109	479	40	3.00
SUMITA - IWATEKEN	IWTH04	175	106	934	101	1.74
DAIGO - IBARAKIKEN	IBRH12	265	200	974	92	1.76

698

699

700 **Table 2.** Stratigraphy and soil properties of profile MYGH09

MYGH09	H-z (m)	$H_j$ (m)	$v_s$ (m s <sup>-1</sup> )	$v_p$ (m s <sup>-1</sup> )	$\rho$ (kg m <sup>-3</sup> )	$\gamma_r$ (‰)
Sand with gravel	2	2	150	400	1800	0.200
	6	4	360	900	1800	0.200
Rock	20	14	360	1660	1900	100
	28	8	490	1660	1900	100
Silt	30.6	2.6	490	1660	1300	0.427
Rock	38	7.4	490	1660	1900	100
	48	10	770	2030	1900	100
Silt	64	16	770	2030	1300	0.427
Rock	80	16	770	2030	1900	100
	86.15	6.15	840	2030	1900	100
	94.27	8.12	840	2030	1900	100
Silt with sand	100	5.73	840	2030	1900	0.427

701

702

703 **Table 3.** Stratigraphy and soil properties of profile FKSH20

FKSH20	H-z (m)	H <sub>j</sub> (m)	v <sub>s</sub> (m s <sup>-1</sup> )	v <sub>p</sub> (m s <sup>-1</sup> )	ρ (kg m <sup>-3</sup> )	γ <sub>r</sub> (‰)
Clay	4	4	350	1500	1200	2.431
	12.3	8.3	350	1500	1200	2.431
Sand with gravel	32	19.7	350	1500	1500	0.368
	60	28	500	1500	1500	0.368
	62.4	2.4	610	1900	1500	0.368
Silt	88	25.6	610	1900	1300	0.427
Rock	109	21	610	1900	1900	100

704

705

706 **Table 4.** Stratigraphy and soil properties of profile IWTH04

IWTH04	H-z (m)	H <sub>j</sub> (m)	v <sub>s</sub> (m s <sup>-1</sup> )	v <sub>p</sub> (m s <sup>-1</sup> )	ρ (kg/m <sup>-3</sup> )	γ <sub>r</sub> (‰)
Clay	1	1	220	440	1200	2.431
Sand	5	4	220	440	1900	0.200
Clay	15	10	400	800	1200	2.431
Rock	49	34	830	2200	2100	100
	106	57	2300	4000	2100	100

707

708

709 **Table 5.** Stratigraphy and soil properties of profile IBRH12

IBRH12	H-z (m)	H <sub>j</sub> (m)	v <sub>s</sub> (m s <sup>-1</sup> )	v <sub>p</sub> (m s <sup>-1</sup> )	ρ (kg/m <sup>3</sup> )	γ <sub>r</sub> (‰)
Rock	6	6	240	550	1700	100
	10	4	560	1900	1700	100
Sand with silt	14	4	560	1900	1550	0.368
Silt	16	2	560	1900	1350	0.427
Sand with silt	20	4	560	1900	1550	0.368
	26	6	850	2450	1550	0.368
Rock	32	6	850	2450	1900	100
Sand with silt	36	4	850	2450	1550	0.368
Rock	40	4	850	2450	1900	100
Silt	46	6	850	2450	1350	0.427
Rock	50	4	850	2450	1900	100
Sand with silt	56	6	850	2450	1550	0.368
Silt	58	2	850	2450	1350	0.427
Rock	74	16	1280	2650	2100	100
Silt	90	16	1120	2550	1350	0.427
Rock	92	2	1120	2550	2100	100
Silt	108	16	1120	2550	1350	0.427
Rock	112	4	1120	2950	2100	100
Silt	120	8	1120	2950	1350	0.427
Sand with silt	126	6	1120	2950	1550	0.368
Silt	136	10	1120	2950	1350	0.427
Rock	150	14	1450	2950	2100	100
Silt	154	4	1250	2700	1350	0.427
Sand with silt	158	4	1250	2700	1550	0.368
Silt	174	16	1250	2700	1350	0.427
Rock	195	21	1700	3000	2100	100
Silt	197	2	1700	3000	1350	0.427
Rock	203	6	1700	3000	2100	100

710

711

712

713 **Table 6.** Acceleration-components recorded downhole during the 2011 Tohoku earthquake

Site code	$a_x$ ( $m\ s^{-2}$ )	$a_y$ ( $m\ s^{-2}$ )	$a_z$ ( $m\ s^{-2}$ )	$a_z / PGA$ (%)
MYGH09	1.26	1.22	1.06	84
FKSH20	1.57	3.56	1.54	43
IWTH04	0.83	0.86	0.73	85
IBRH12	1.21	1.08	0.73	60

714

715 **Table 7.** Numerical and recorded acceleration and velocity components of the 2011 Tohoku  
716 earthquake at the surface of selected soil profiles

Site code		$a_x$ ( $m\ s^{-2}$ )	$a_y$ ( $m\ s^{-2}$ )	$a_z$ ( $m\ s^{-2}$ )	$v_x$ ( $m\ s^{-1}$ )	$v_y$ ( $m\ s^{-1}$ )	$v_z$ ( $m\ s^{-1}$ )
	Record	3.15	<b>3.23</b>	2.91	<b>0.31</b>	0.30	0.23
MYGH09	Filtered	3.05	<b>3.07</b>	2.22	<b>0.31</b>	0.30	0.23
	1D-3C	3.10	2.84	3.27	0.41	0.32	0.26
	Record	3.94	<b>6.60</b>	2.66	0.44	<b>1.09</b>	0.15
FKSH20	Filtered	3.90	<b>6.60</b>	2.21	0.44	<b>1.09</b>	0.15
	1D-3C	2.72	2.73	3.99	0.35	0.68	0.18
	Record	3.33	<b>3.84</b>	<b>3.88</b>	0.20	<b>0.24</b>	0.09
IWTH04	Filtered	3.10	<b>3.84</b>	<b>2.78</b>	0.20	<b>0.24</b>	0.09
	1D-3C	3.36	2.78	7.15	0.19	0.19	0.16
	Record	<b>6.04</b>	5.26	5.58	<b>0.29</b>	0.26	0.13
IBRH12	Filtered	<b>5.78</b>	5.25	4.31	<b>0.29</b>	0.26	0.13
	1D-3C	3.61	3.77	2.50	0.23	0.19	0.14

717

718

719

720

721

722

723 **Table 8.** Anderson's Good-of-Fit scores (NIA, shape of the normalized integral of acceleration  
724 squared with respect to Arias intensity; NIE, shape of the normalized integral of velocity  
725 squared with respect to the energy integral; IA, Arias intensity; IE, energy integral; PA, peak  
726 acceleration; PV, peak velocity; PD, peak displacement; SA, acceleration response spectrum;  
727 FFT, Fourier spectrum; CC, cross correlation) for numerical seismograms of the 2011 Tohoku  
728 earthquake at the surface of selected soil profiles : Excellent (A), Good (B), Fair (C), Poor (D)

Site code		NIA	NIE	IA	IE	PA	PV	PD	SA	FFT	CC
MYGH09	x	A	A	D	C	A	A	D	C	D	D
	y	A	A	D	A	A	A	B	A	D	D
	z	A	A	D	A	A	A	A	A	D	D
FKSH20	x	A	A	A	C	A	A	D	A	D	D
	y	A	C	A	D	D	B	D	D	D	D
	z	B	A	D	C	C	A	A	C	D	D
IWTH04	x	A	A	D	A	A	A	D	A	D	D
	y	B	A	D	A	A	A	A	A	D	D
	z	A	B	D	D	D	C	A	D	C	D
IBRH12	x	A	A	C	A	B	A	D	B	D	D
	y	A	A	A	B	A	A	D	A	D	D
	z	B	A	B	B	C	A	A	C	D	D

729

730

731

732

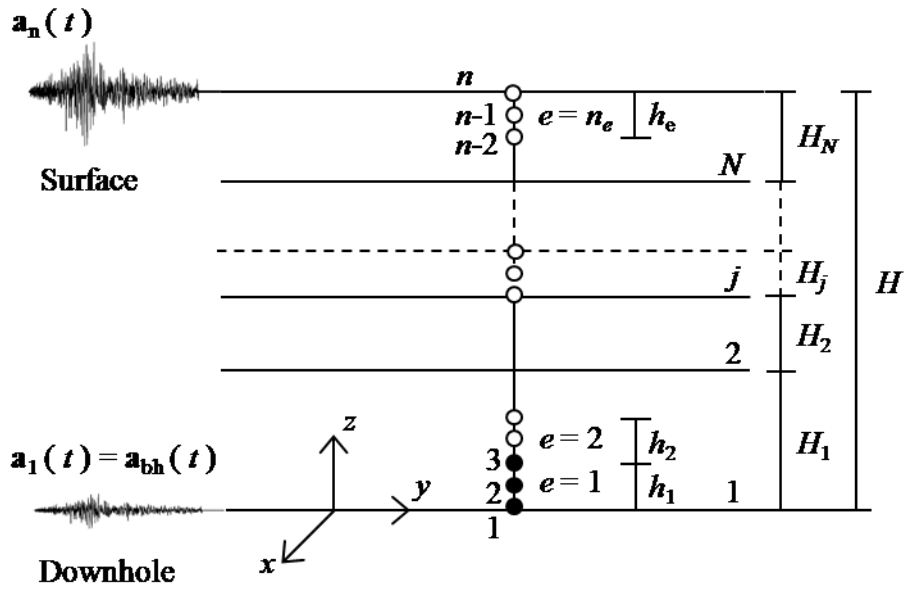
733

734

735

736

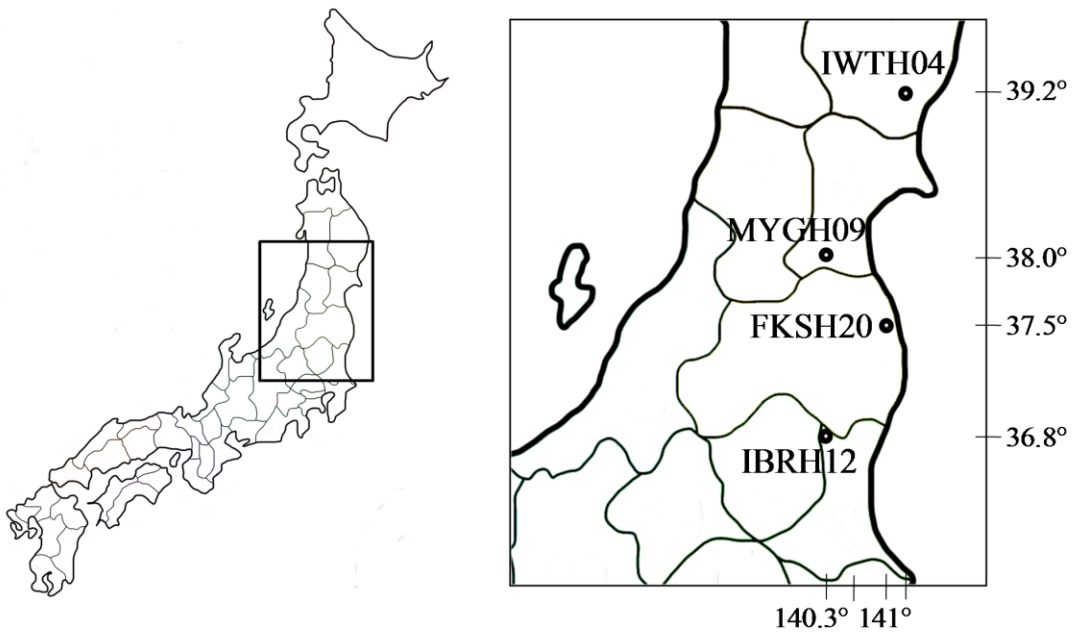
737



738

739 **Figure 1.** Spatial discretization of a horizontally layered soil excited at its base (node 1) by a  
 740 three-component borehole seismic record.

741



742

743 **Figure 2.** Location of analyzed soil profiles in the Tohoku area (Japan), KiK-Net accelerometers  
 744 being placed at the surface and at depth.

745  
746  
747  
748  
749  
750  
751  
752  
753  
754  
755  
756  
757  
758  
759  
760  
761  
762  
763  
764  
765  
766  
767

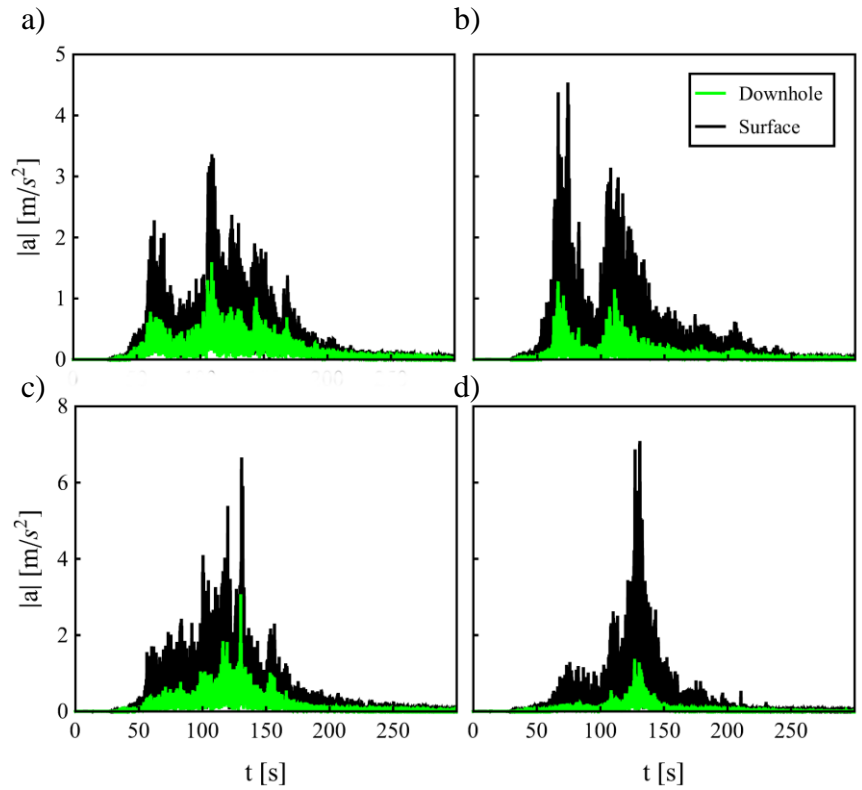
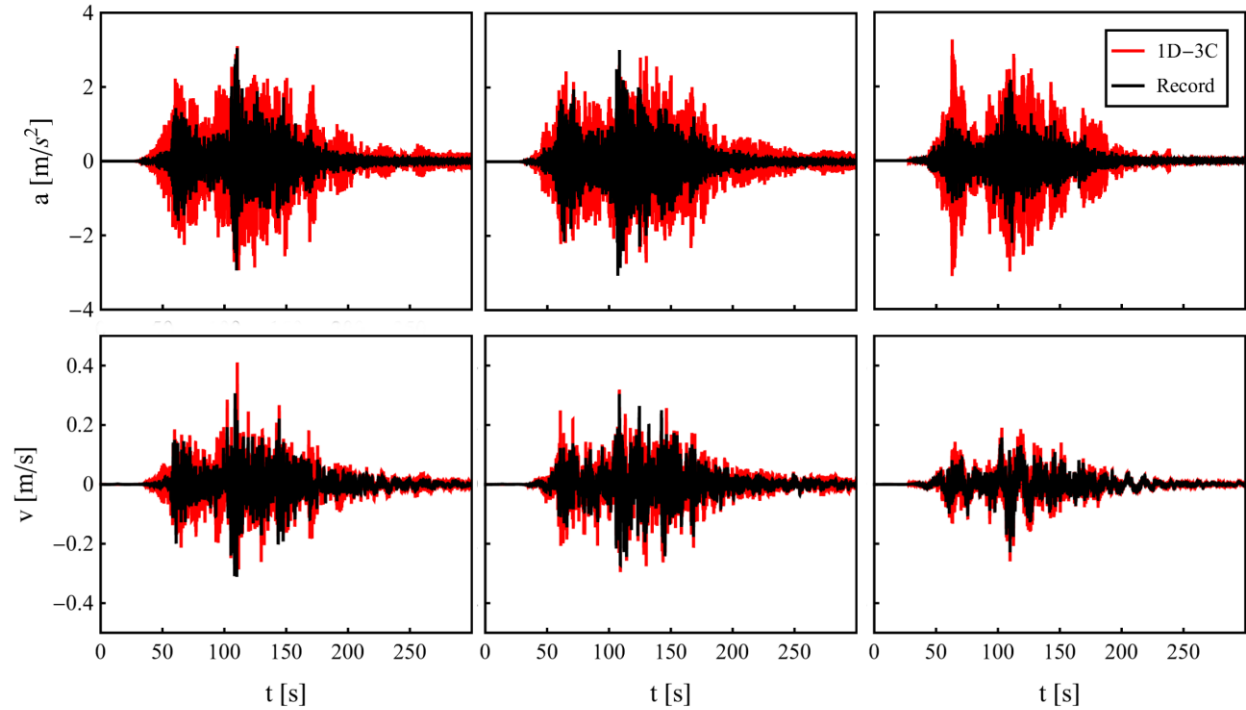


**Figure 3.** Time history of measured acceleration modulus at the base and surface of soil profiles MYGH09 (a), IWTH04 (b), FKSH20 (c) and IBRH12 (d), during the 2011 Tohoku earthquake.



768

769 **Figure 4.** Time history of measured and numerical acceleration (top) and velocity (bottom), in  
 770 directions NS (left), EW (middle) and UD (right), at the surface of soil profile MYGH09, during  
 771 the 2011 Tohoku earthquake.

772

773

774

775

776

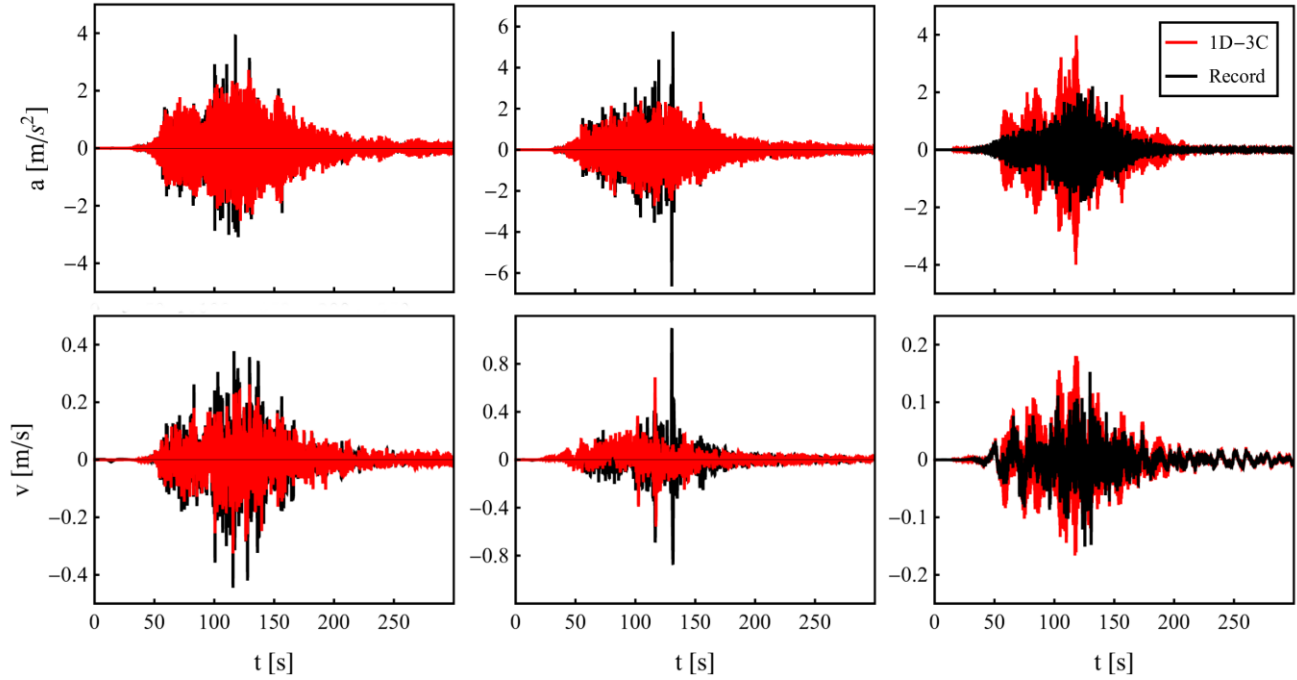
777

778

779

780

781



782

783 **Figure 5.** Time history of measured and numerical acceleration (top) and velocity (bottom), in  
 784 directions NS (left), EW (middle) and UD (right), at the surface of soil profile FKSH20, during  
 785 the 2011 Tohoku earthquake.

786

787

788

789

790

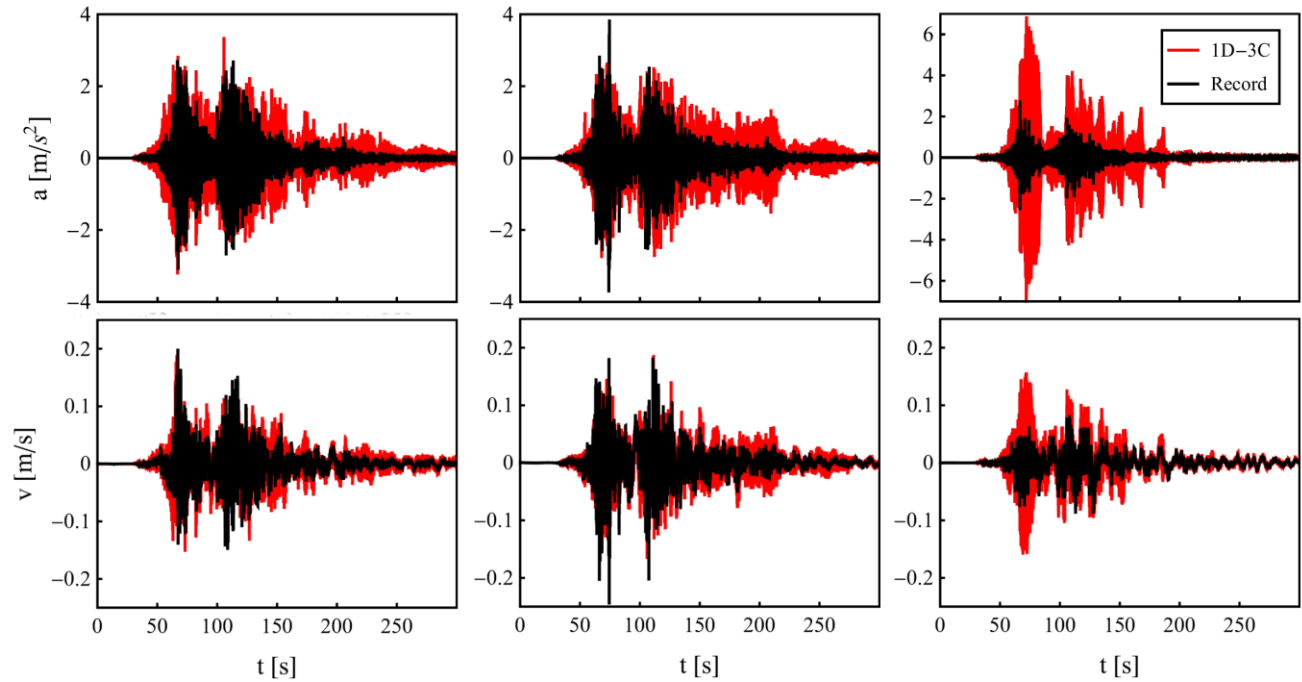
791

792

793

794

795



796

797 **Figure 6.** Time history of measured and numerical acceleration (top) and velocity (bottom), in  
 798 directions NS (left), EW (middle) and UD (right), at the surface of soil profile IWTH04, during  
 799 the 2011 Tohoku earthquake.

800

801

802

803

804

805

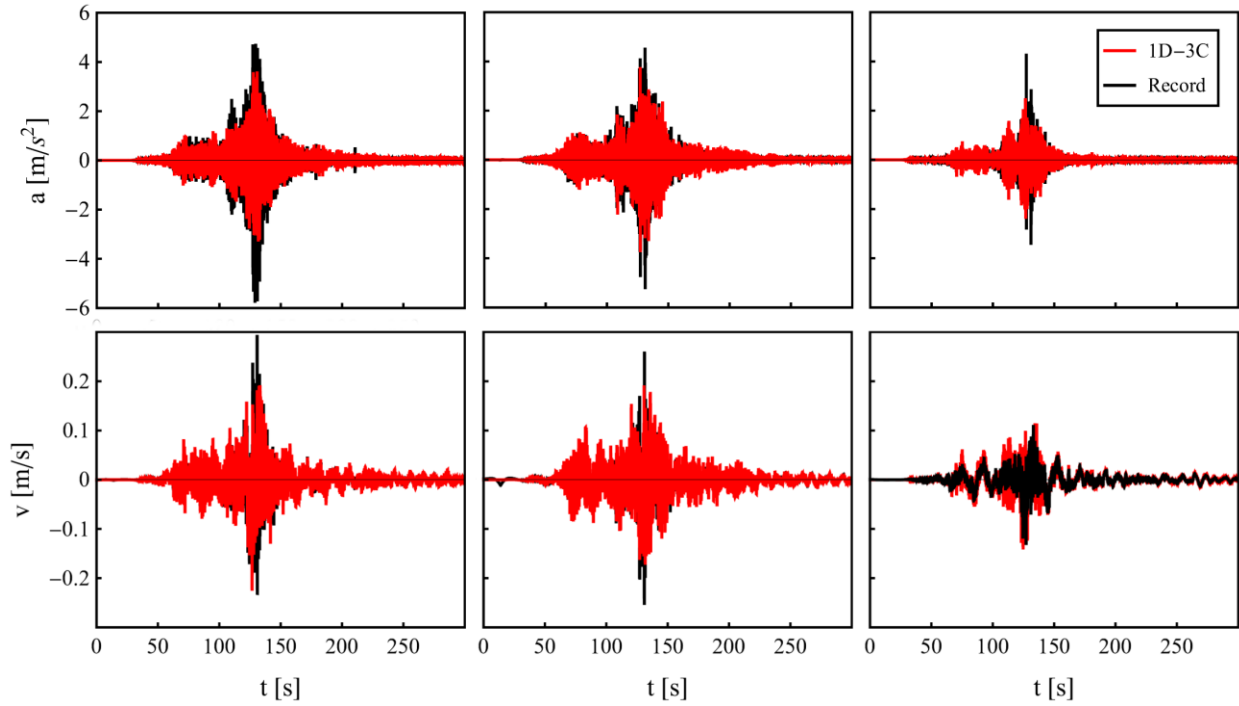
806

807

808

809

810



811

812 **Figure 7.** Time history of measured and numerical acceleration (top) and velocity (bottom), in  
 813 directions NS (left), EW (middle) and UD (right), at the surface of soil profile IBRH12, during  
 814 the 2011 Tohoku earthquake.

815

816

817

818

819

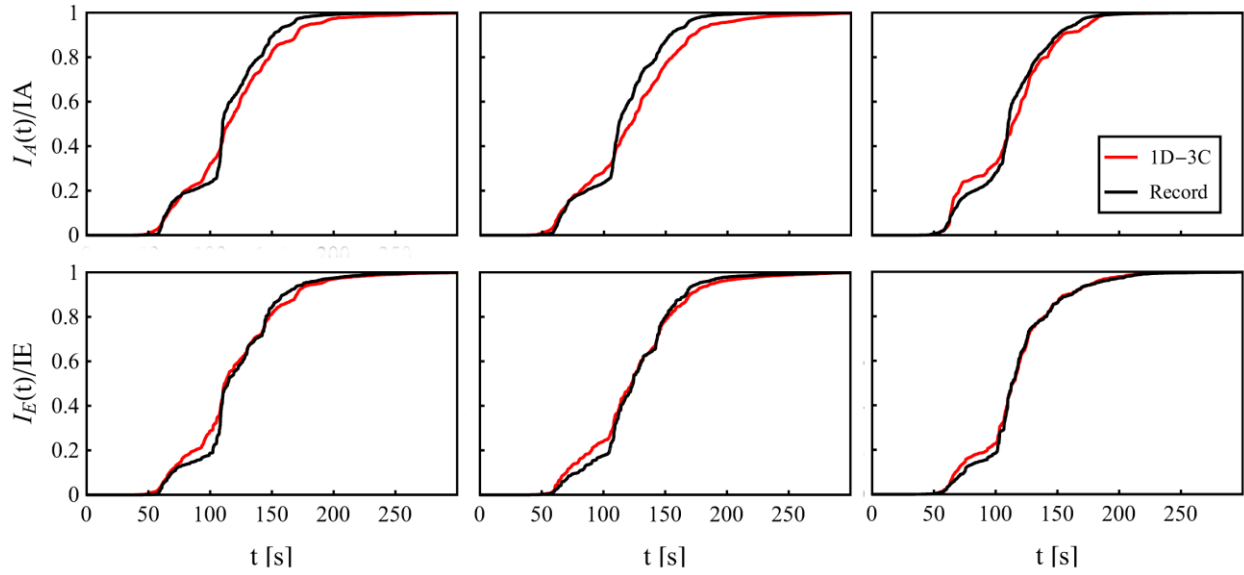
820

821

822

823

824



825

826 **Figure 8.** Normalized integral of acceleration (top) and velocity (bottom) squared for soil profile

827 MYGH09.

828

829

830

831

832

833

834

835

836

837

838

839

840

841  
842  
843  
844  
845  
846  
847  
848  
849  
850  
851  
852  
853  
854  
855  
856  
857  
858  
859  
860  
861  
862  
863

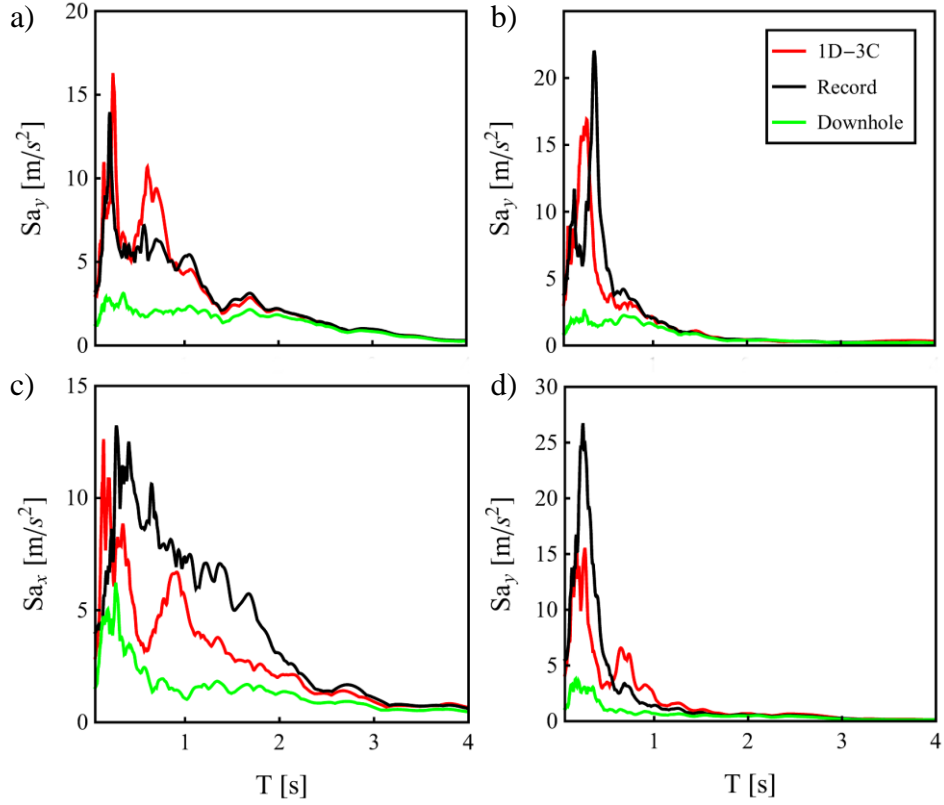
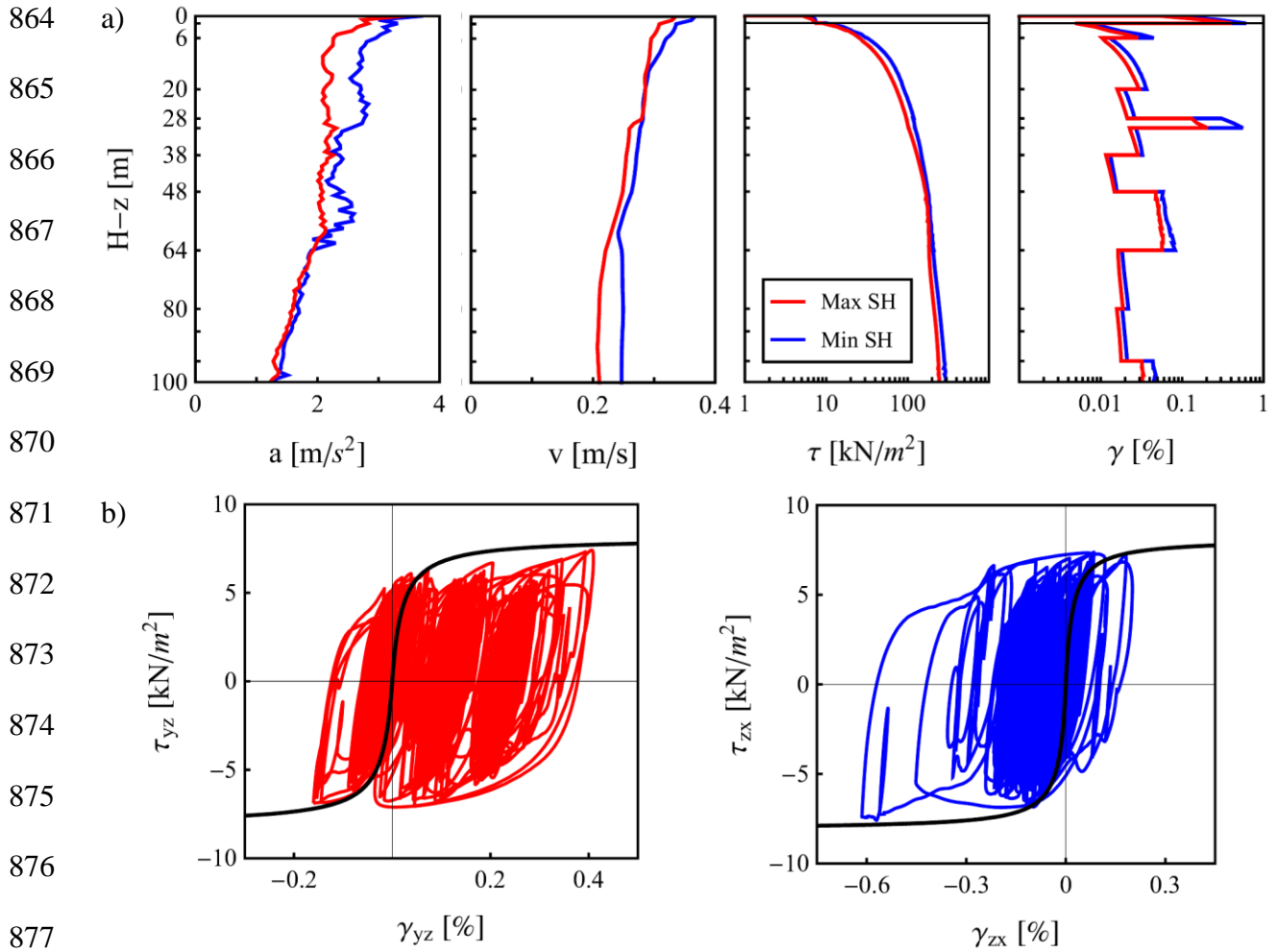
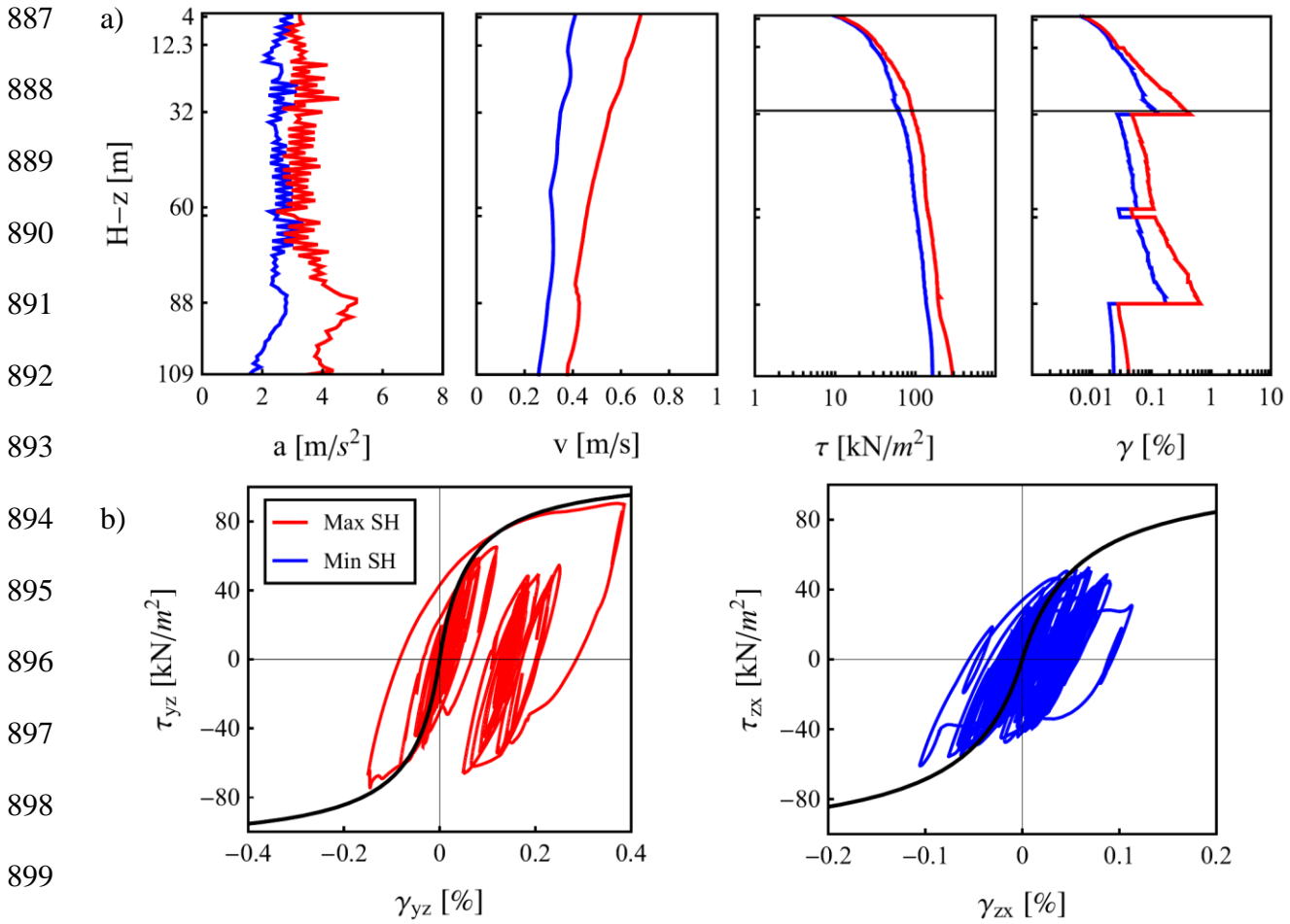


**Figure 9.** Numerical best fitted spectra, for soil profiles MYGH09 (a), IWTH04 (b), FKSH20 (c) and IBRH12 (d), and spectra corresponding to records at the bottom and at the surface.



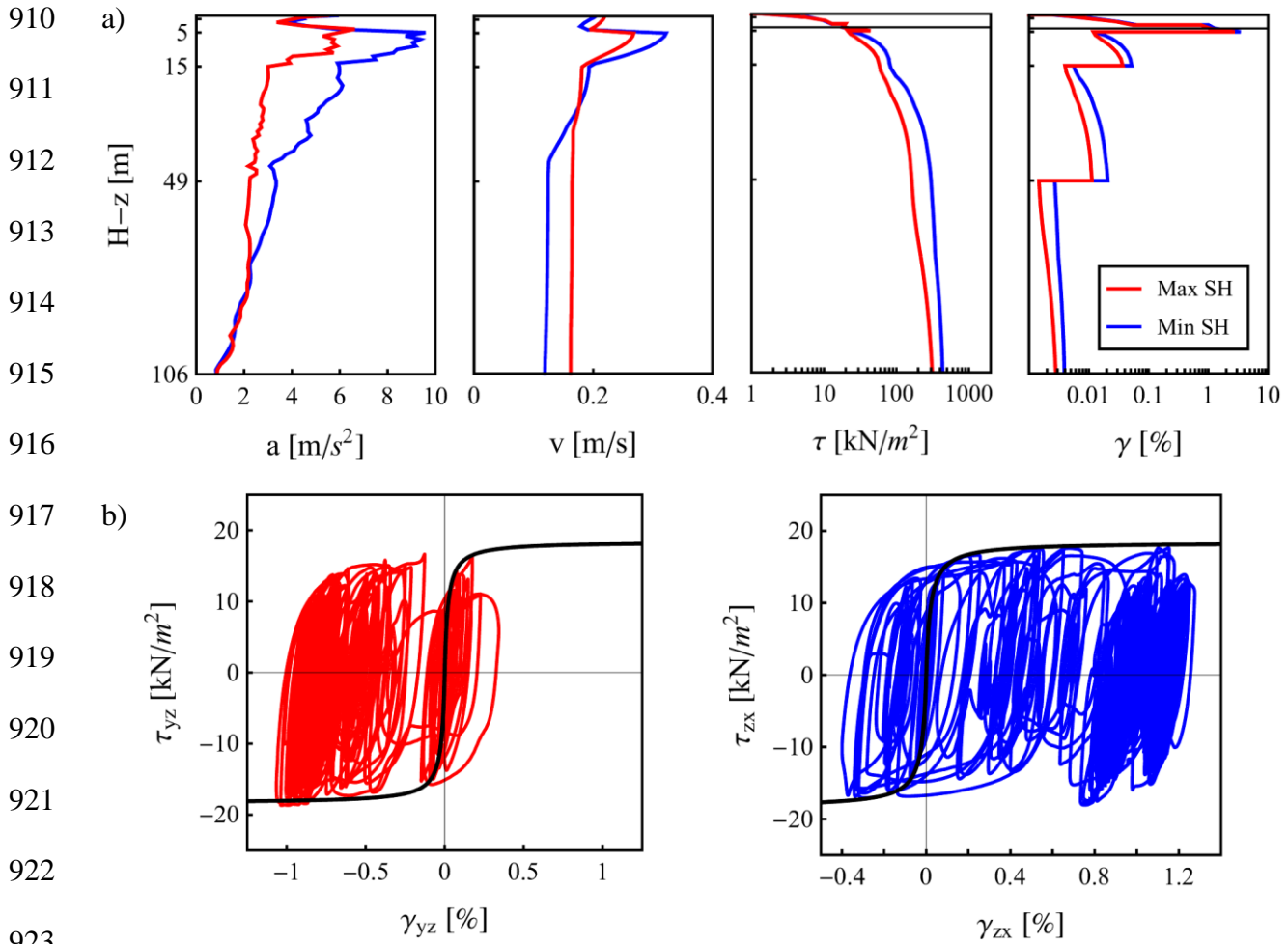
878 **Figure 10.** 1D-3C seismic response of soil profile MYGH09, during the 2011 Tohoku  
 879 earthquake, in both horizontal directions of motion: acceleration, velocity, strain and stress with  
 880 depth (a); shear stress-strain loops at 2 m depth (b).

881  
 882  
 883  
 884  
 885  
 886



900 **Figure 11.** 1D-3C seismic response of soil profile FKSH20, during the 2011 Tohoku earthquake,  
 901 in both horizontal directions of motion: acceleration, velocity, strain and stress with depth (a);  
 902 shear stress-strain loops at 31 m depth (b).

903  
 904  
 905  
 906  
 907  
 908  
 909



924 **Figure 12.** 1D-3C seismic response of soil profile IWTH04, during the 2011 Tohoku earthquake,  
 925 in both horizontal directions of motion: acceleration, velocity, strain and stress with depth (a);  
 926 shear stress-strain loops at 4 m depth (b).

927

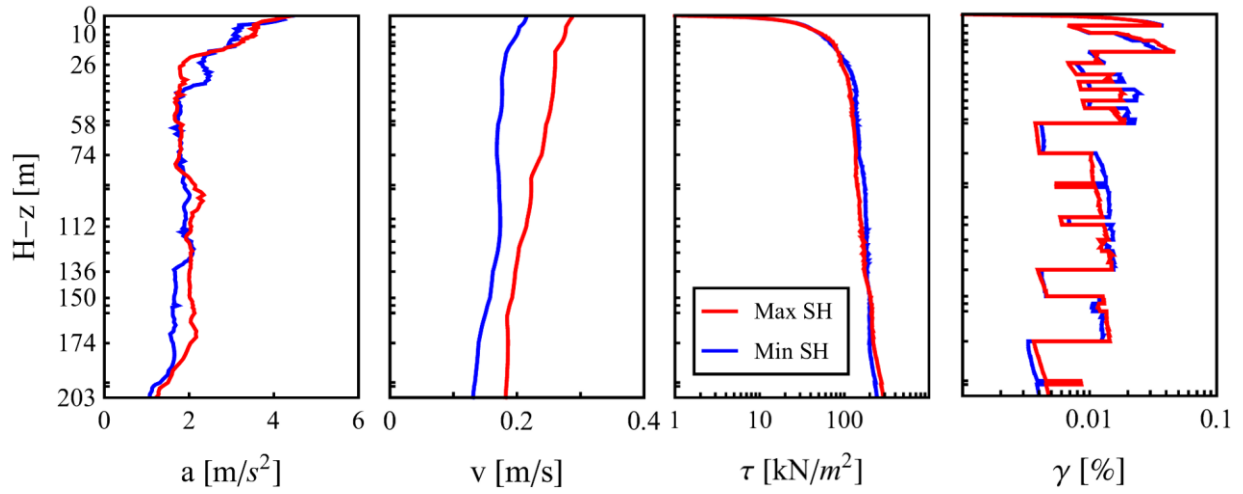
928

929

930

931

932



933

934 **Figure 13.** 1D-3C seismic response of soil profile IBRH12, during the 2011 Tohoku earthquake,

935 in both horizontal directions of motion: acceleration, velocity, strain and stress with depth.

936

937

938

939

940

941

942

943

944

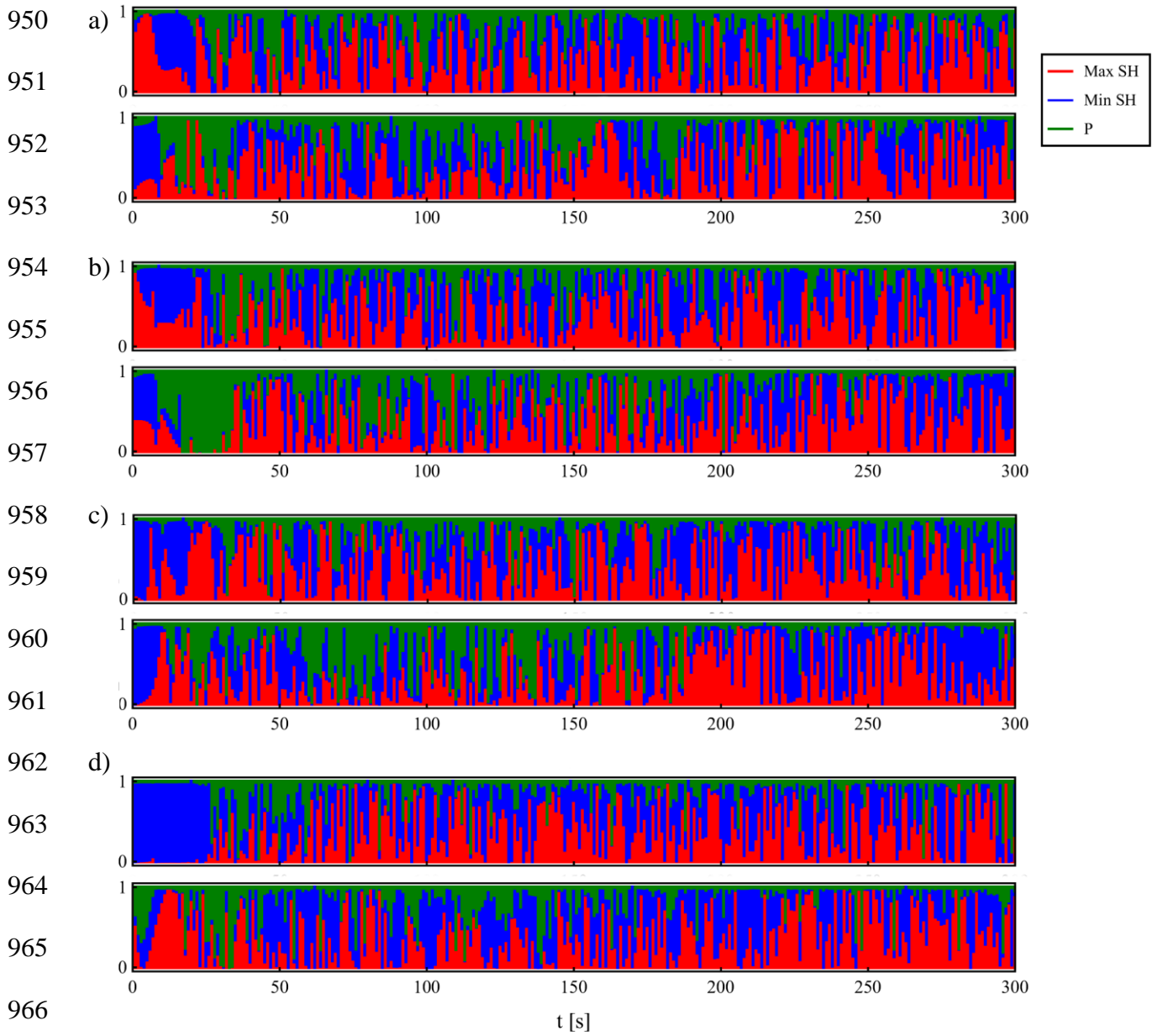
945

946

947

948

949



967 **Figure 14.** Recorded (top) and numerical (bottom) normalized polarization of seismic waves in  
 968 terms of acceleration at the surface of soil profiles MYGH09 (a), FKSH20 (b), IWTH04 (c) and  
 969 IBRH12 (d). Max SH is the PGA horizontal direction and P is the vertical direction.

970

971

972

973 **APPENDIX**

974 The assembled  $(3n \times 3n)$ -dimensional mass matrix  $\mathbf{M}$  and the  $3n$ -dimensional vector of  
 975 internal forces  $\mathbf{F}_{\text{int}}$ , in equation (2), result from the assemblage of  $(9 \times 9)$ -dimensional matrices  
 976  $\mathbf{M}^e$  and vectors  $\mathbf{F}_{\text{int}}^e$ , respectively, corresponding to the element  $e$ , which are expressed as

977 
$$\mathbf{M}^e = \rho_e \int_0^{h_e} \mathbf{N}^T \mathbf{N} dz \quad \mathbf{F}_{\text{int}}^e = \int_0^{h_e} \mathbf{B}^T \boldsymbol{\sigma} dz \quad (13)$$

978 where  $h_e$  is the finite element length and  $\rho_e$  is the soil density assumed constant in the element.

979 The 6-dimensional stress and strain vectors, defined according to the hypothesis of infinite  
 980 horizontal soil, are

981 
$$\begin{aligned} \boldsymbol{\sigma} &= \begin{bmatrix} \sigma_{xx} & \sigma_{yy} & 0 & \tau_{yz} & \tau_{zx} & \sigma_{zz} \end{bmatrix}^T \\ \boldsymbol{\varepsilon} &= \begin{bmatrix} 0 & 0 & 0 & \gamma_{yz} & \gamma_{zx} & \varepsilon_{zz} \end{bmatrix}^T \end{aligned} \quad (14)$$

982 In equation (2),  $\mathbf{N}(z)$  is the  $(3 \times 9)$ -dimensional shape function matrix. Integrals in equation (2)  
 983 are solved using the change of coordinates  $z = (1 + \zeta)h_e/2$  with  $dz = h_e/2 d\zeta$ , where  $\zeta \in [-1, 1]$   
 984 is the local coordinate in the element, and the Gaussian numerical integration. The shape  
 985 function matrix is defined, in local coordinates, as

986 
$$\mathbf{N}(\zeta) = \begin{bmatrix} N_1 & N_2 & N_3 & & & & & & \\ & & & N_1 & N_2 & N_3 & & & \\ & & & & & & N_1 & N_2 & N_3 \end{bmatrix} \quad (15)$$

987 According to Cook *et al.* (2002),  $N_1 = -\zeta(1 - \zeta)/2$ ,  $N_2 = (1 - \zeta^2)$  and  $N_3 = \zeta(1 + \zeta)/2$  are the  
 988 quadratic shape functions corresponding to the three-node line element used to discretize the soil  
 989 column. The terms of the  $(6 \times 9)$ -dimensional matrix  $\mathbf{B}(z)$  are the spatial derivatives of the  
 990 shape functions, according to compatibility conditions and to the hypothesis of no strain

991 variation in the horizontal directions  $x$  and  $y$ . The strain vector is defined as  $\boldsymbol{\varepsilon} = \partial \mathbf{u}$  (Cook *et al.*  
 992 2002), where the terms of  $\mathbf{u}$  are the displacements in  $x$ -,  $y$ - and  $z$ -direction and  $\partial$  is a matrix of  
 993 differential operators defined in such a way that compatibility equations are verified. Matrix  
 994  $\mathbf{B} = \partial \mathbf{N}$  thus reads as follows:

$$995 \quad \mathbf{B} = \begin{bmatrix} \mathbf{0}_3 & \mathbf{0}_3 & \mathbf{0}_3 & \mathbf{0}_3 & \mathbf{B}_z & \mathbf{0}_3 \\ \mathbf{0}_3 & \mathbf{0}_3 & \mathbf{0}_3 & \mathbf{B}_z & \mathbf{0}_3 & \mathbf{0}_3 \\ \mathbf{0}_3 & \mathbf{0}_3 & \mathbf{0}_3 & \mathbf{0}_3 & \mathbf{0}_3 & \mathbf{B}_z \end{bmatrix}^T \quad (16)$$

996 where  $\mathbf{0}_3$  is a 3-dimensional null vector and  $\mathbf{B}_z = [\partial N_1/\partial z \quad \partial N_2/\partial z \quad \partial N_3/\partial z]^T$  with  
 997  $\partial N_i/\partial z = (\partial N_i/\partial \zeta)(\partial \zeta/\partial z)$  for  $i = 1, 2, 3$  and  $\partial \zeta/\partial z = 2/h_e$ .

998 The  $(3n \times 3n)$ -dimensional stiffness matrix  $\mathbf{K}_k^i$ , in equation (3), is obtained by assembling  
 999  $(9 \times 9)$ -dimensional matrices as follows, with respect to element  $e$  :

$$1000 \quad k_k^{e,i} = \int_0^{h_e} \mathbf{B}^T \mathbf{E}_k^i \mathbf{B} dz \quad (17)$$

1001 The  $(6 \times 6)$ -dimensional tangent constitutive matrix  $\mathbf{E}_k^i$  is evaluated by the incremental  
 1002 constitutive relationship given by

$$1003 \quad \Delta \boldsymbol{\sigma}_k^i = \mathbf{E}_k^i \Delta \boldsymbol{\varepsilon}_k^i \quad (18)$$

1004 According to Joyner (1975), the actual strain level and the strain and stress values at the  
 1005 previous time step allow to evaluate the tangent constitutive matrix  $\mathbf{E}_k^i$  and the stress increment

$$1006 \quad \Delta \boldsymbol{\sigma}_k^i = \Delta \boldsymbol{\sigma}_k^i(\boldsymbol{\varepsilon}_k^i, \boldsymbol{\varepsilon}_{k-1}, \boldsymbol{\sigma}_{k-1}).$$